Nuclear linear response to electroweak interactions in a relativistic theory for ^{16}O

Michael W. Price*
Nuclear Theory Center and Department of Physics, Indiana University, Bloomington, Indiana 47405 and Center for Naval Analyses, Alexandria, Virginia 22302

G. E. Walker
Nuclear Theory Center and Department of Physics, Indiana University, Bloomington, Indiana 47405
(Received 6 July 1988)

The linear response of the ^{16}O nucleus to an external electroweak current is studied in a relativistic model. The relativistic form for the nuclear linear response is applied using the random-phase approximation, Dirac-Hartree single-nucleon orbitals obtained along with Lorentz-vector and scalar self-consistent meson mean fields, and various particle-hole residual interactions. Form factors for inelastic electron scattering are combined into complexes and compared with experiments and previous nonrelativistic predictions. The agreement with electron scattering experiments is of similar quality for both nonrelativistic and relativistic theories with no obvious signature obtained motivating the superiority of a relativistic treatment. For weak interactions, the relativistic approach yields a considerable variation in predictions depending on the residual interaction adopted and whether pseudovector or pseudoscalar πNN coupling is assumed.

I. INTRODUCTION

There has been considerable recent interest in the role of relativistic dynamics in nuclear structure and nuclear reactions. The application of relativistic quantum field theory to nuclei[1–3] and the study of relativistic nuclear Dirac phenomenology[4] has led, as examples, to one explanation of (a) the large nuclear effective single-particle spin-orbit potential and (b) the spin observables in intermediate energy proton-nucleus elastic scattering experiments. The relativistic models are characterized by large (300–400 MeV) nuclear mean fields. The deep attractive mean field due to scalar-isoscalar meson exchange is largely canceled by a repulsion associated with vector meson exchange. This results in the relatively small ($\sim$50 MeV) nuclear potential commonly adopted in nonrelativistic nuclear models. It is important to determine the validity of the main features of the present relativistic models and also to determine whether it is more fertile to use relativistic models or to adopt standard nonrelativistic approaches treating relativistic effects as correction terms.

The presence of the large attractive scalar field results in the prediction of a small effective nucleon mass ($M^* \sim 0.6M$) in the nuclear interior. This, in turn, leads to an enhancement of the lower components in the Dirac single-nucleon orbitals. Thus there is interest in studying static nuclear properties (such as magnetic moments) or reactions (involving, for example, the nuclear linear response) where the lower-components are expected to play a non-negligible role. A significant difference between relativistic model predictions and standard nonrelativistic predictions with the relativistic predictions confirmed by experiment would be an indication of the fertility of the relativistic approach.

Because of complications associated with strongly interacting probe-nucleus reactions, the most straightforward tests of the relativistic approach might be expected from studies of electroweak nuclear reactions. Even for electroweak reactions, isolation of effects associated with the enhancement of the lower components is apparently not straightforward. Many transition densities are surface peaked where effective mass enhancement effects are small. Relativistic prediction of magnetic moments or magnetic elastic electron scattering must include corrections due to "backflow" contributions in the closed-shell $\pm$ one nucleon system.[5] When these corrections are included the large enhancements of magnetic moment characteristic of relativistic models are reduced and the results are close to the traditional Schmidt lines. Large correction terms are expected for *isoscalar* matrix elements. Therefore, in the current investigation we have studied the *isovector* linear response of ^{16}O to electroweak probes. Although we make contact with experimental results we also study the sensitivity of the results to changes in the residual interaction and the approximation involved in evaluating the nuclear linear response. Specifically we have studied the predicted energy level scheme for (particle-hole) excited states in ^{16}O as a function of the assumed relativistic baryon-baryon interaction, treatment of the nuclear continuum, and procedure for obtaining single-particle energies. We have then used the obtained wave functions and relativistic transition operators to make predictions of transition rates for electron scattering and muon capture on ^{16}O, and beta decay on ^{16}N. Especially in the case of weak interactions there exist identifiable significant differences between the present relativistic treatment and previous nonrelativistic calculations or other less complete relativistic calculations. For these cases we have investigated which effects arise from the relativistic treatment and which effects are due to a more realistic treatment of the nuclear continu-

um (which could have also been included in earlier nonrelativistic calculations).

In the next section we briefly summarize the formulas used to evaluate the nuclear linear response in the relativistic formalism. Also in this section we discuss the various different prescriptions, input parameters, and particle-hole interactions adopted to obtain the nuclear polarization propagator required to calculate the electroweak linear response function.

The electroweak transition-matrix elements require the evaluation of matrix elements involving single-baryon Dirac-Hartree orbitals. Thus the electroweak nuclear transition operators are expressed in *full* relativistic form. The definitions and explicit forms for the operators used in this investigation are summarized in the Appendix. The general expressions used to obtain the differential cross sections for (e,e'), beta decay lifetimes and muon capture rates are given in Sec. II.

The results for the predicted excitation spectrum, electron scattering form factors, muon capture, and beta-decay rates are given in Sec. III. In this section, we also compare the predictions with experiment and previous nonrelativistic results.

Finally, in Sec. IV we briefly summarize results and discuss the main conclusions to be drawn from this investigation.

II. PROCEDURES AND FORMULAS

A. Linear response in the random-phase approximation

We study the nuclear linear response to an electroweak perturbation. The nuclear linear response is determined by the density correlation function (or polarization propagator) which is defined by[6,7]

$$i\pi_{\lambda\mu,\alpha\beta}(t-t') \equiv \langle\Psi^0|T[C^\dagger_{H\mu}(t)C_{H\lambda}(t)C^\dagger_{H\alpha}(t')C_{H\beta}(t')]|\Psi^0\rangle \ , \quad (1)$$

where $|\Psi^0\rangle$ is the exact normalized Heisenberg ground state of the assumed Hamiltonian. The Heisenberg creation and destruction operators $(C^\dagger, C)$ appearing in the time-ordered product in Eq. (1) are taken to refer to single-particle Hartree orbitals in our application. By considering the Fourier transform, $\pi(\omega)$, and inserting a complete set of Heisenberg representation eigenstates, $|\Psi^n\rangle$, of the Hamiltonian, the Lehmann representation of $\pi(\omega)$ is obtained:

$$\pi_{\lambda\mu,\alpha\beta}(\omega)=\hbar\sum_n\left[\frac{\langle\Psi^0|C^\dagger_{H\mu}C_{H\lambda}|\Psi^n\rangle\langle\Psi^n|C^\dagger_{H\alpha}C_{H\beta}|\Psi^0\rangle}{\hbar\omega-(E_n-E_0)+i\eta}-\frac{\langle\Psi^0|C^\dagger_{H\alpha}C_{H\beta}|\Psi^n\rangle\langle\Psi^n|C^\dagger_{H\mu}C_{H\lambda}|\Psi^0\rangle}{\hbar\omega+(E_n-E_0)-i\eta}\right] . \quad (2)$$

The poles of π yield the energy spectrum of the nucleus, including the final states induced by the electroweak perturbation. In order to explicitly evaluate $\pi(\omega)$ the procedure is to transform to the interaction representation and consider diagrams involving appropriate time orderings of the interaction Hamiltonian (here involving meson-baryon interactions) that are not already included in obtaining the Hartree orbitals.[7] The detailed form of the interaction Hamiltonian depends on the theory under consideration. In most nonrelativistic applications one assumes an interaction that is a delta function in $(t-t')$ [see Eq. (1)]. Such an assumption suppresses meson propagation effects. If meson propagation effects are included, relativistically or nonrelativistically, the density correlation function has a nontrivial frequency dependence. In what follows we assume that the energies of the excited states under investigation are much smaller than the masses of the exchanged mesons, and that it is therefore a reasonable approximation to ignore retardation corrections. We also drop terms associated with nucleon-antinucleon pair excitations. Along with these approximations we adopt the standard random-phase approximation (RPA) for evaluation of the particle-hole polarization propagator.[7] Adopting this set of approximations one may keep the full Dirac four-component nature of the single-particle orbitals and the particle-hole interaction and still obtain the usual RPA equations for the Dirac particle-hole admixture amplitudes.

We use standard angular momentum and isospin coupling and label the nth excited state of the nucleus as $|\Psi_{JT}\rangle$, where $J(T)$ denotes the total angular momentum (isospin) of the nuclear excited state. In the RPA approximation $|\Psi_{JT}\rangle$ is obtained from the exact ground state $|\Psi^0\rangle$ by creating or destroying a particle-hole pair. Thus the excited state can be written[7]

$$|\Psi^n_{JT}\rangle=\sum_{ab}\psi^*_{JT}(ab)\hat{\xi}^\dagger(abJT)|\Psi^0\rangle + \sum_{ab}\phi^n_{JT}(ab)\hat{\xi}(abJT)|\Psi^0\rangle \ , \quad (3)$$

where $\xi^\dagger(\xi)$ is a particle (a) -hole (b) pair creation (destruction) operator appropriate for a pair having total angular momentum J and isospin T. The RPA admixture amplitudes, ψ^n_{JT} and ϕ^n_{JT}, can be determined by solving the set of coupled algebraic equations:[7]

$$\{[E_0+(\epsilon_a-\epsilon_b)]-E_n\}\psi^n_{JT}(ab) + \sum_{lm}[v^{JT}_{ab,lm}\psi^n_{JT}(lm)+u^{JT}_{ab,lm}\phi^n_{JT}(lm)]=0 \quad (4a)$$

and

$$\{[E_0-(\epsilon_a-\epsilon_b)]-E_n\}\phi^n_{JT}(ab) - \sum_{lm}[v^{JT*}_{ab,lm}\phi^n_{JT}(lm)+u^{JT*}_{ab,lm}\psi^n_{JT}(lm)]=0 \ . \quad (4b)$$

In Eqs. (4a) and (4b) above the (ϵ_a,ϵ_b) refer to single-particle Hartree energies and

$$v^{JT}_{ab,lm} = -\sum_{J'T'} (2J'+1)(2T'+1) \begin{bmatrix} j_m & j_a & J' \\ j_b & j_l & J \end{bmatrix} \begin{bmatrix} \frac{1}{2} & \frac{1}{2} & T' \\ \frac{1}{2} & \frac{1}{2} & T \end{bmatrix} \times [\langle lbJ'T'|V|amJ'T'\rangle - (-1)^{1+T'+j_a+J_m+J'} \langle lbJ'T'|V|maJ'T'\rangle] , \quad (5a)$$

with

$$u^{JT}_{ab,lm} = (-1)^{1/2-1/2-T}(-1)^{j_m-j_l-J} v^{JT}_{ab,ml} . \quad (5b)$$

The single-particle wave functions used in evaluating the matrix elements of the effective N-N interaction V are Dirac-Hartree orbitals associated with Hartree single-particle energy eigenvalues ϵ. The effective N-N interaction V is written in the general Dirac form

$$V(1,2) = A_S + A_V\gamma^\mu(1)\gamma_\mu(2) + A_{PS}\gamma^5(1)\gamma_5(2) + A_{AV}\gamma^5(1)\gamma^\mu(1)\gamma_5(2)\gamma_\mu(2) + A_T\sigma^{\mu\nu}(1)\sigma_{\mu\nu}(2) , \quad (6)$$

where the A's are functions of Lorentz invariants and isospin. The Hartree orbitals, single-particle energies, and effective interaction $V(1,2)$ comprise the required input for solving the nonsymmetric matrix eigenvalue problem represented in Eqs. (4a) and (4b). The determined eigenvectors contain the RPA particle-hole (p-h) admixture amplitudes ψ and ϕ. The corresponding eigenvalues are the nuclear excited state energies. The input will be discussed in more detail below.

The transition amplitude for a one-body operator $\hat{T}_{JT}$ defined in the nuclear many-body space, can be determined, given the RPA admixture amplitudes, via[7]

$$\langle \Psi^n_{JT}\|\hat{T}_{JT}\|\Psi^0\rangle = \sum_{ab} \{\langle a\|T_{JT}\|b\rangle \psi^n_{JT}(ab) + (-1)^{1/2-1/2-T}(-1)^{j_b-j_a-J} \times \langle b\|T_{JT}\|a\rangle \phi^n_{JT}(ab)\} , \quad (7)$$

where the matrix elements are doubly reduced in angular momentum and isospin space.

Note that the single-nucleon orbitals (a,b) in Eq. (7) are of the Dirac type so that the transition operator in Eq. (7) is kept in its full relativistic form. The transition operators appropriate for electron scattering, beta decay, and muon capture applications are discussed later in this section and the Appendix.

B. Dirac-Hartree single particle orbitals

The RPA Eqs. (4a) and (4b) are an infinite set of coupled linear algebraic equations. Reducing the problem to a finite set of equations requires that one limit the number of p-h configurations contributing to the excited states under consideration. We adopt the standard approximation for the low-lying excited states studied here by restricting the sum over particle-hole pairs, lm, in Eqs. (4a) and (4b) to particle states l in the low-lying unfilled valence shell(s) and hole states m, in the highest filled orbitals for the closed-shell ^{16}O nucleus.

In this investigation the single-nucleon Dirac-Hartree wave functions of Horowitz and Serot[2] are adopted for the pure particle-hole basis states. These single-nucleon orbitals are obtained using a Hartree approximation wherein the nucleon orbitals and the σ and ω meson mean fields are determined self-consistently. The procedure used[3] is to assume a Lagrangian containing coupled meson and nucleon fields. The meson fields are treated in the mean-field approximation. For example, for nuclei possessing good parity a typical mean-field Lagrangian is given by[1]

$$\mathcal{L} = \bar{\psi}[i\gamma_\mu\partial^\mu - g_\omega\gamma^0 V_0 - \tfrac{1}{2}g_\rho\tau_3\gamma^0 b_0 - e\tfrac{1}{2}(1+\tau_3)\gamma^0 A_0 - (M - g_\sigma\phi_0)]\psi + \text{pure mesonic} + \text{electromagnetic Coulomb couplings} + \text{counter terms} , \quad (8)$$

where ψ is the nucleon field, M is the nucleon mass, A_0 is the Coulomb potential, and V_0, b_0, and ϕ_0 represent the isoscalar vector meson (ω), isovector vector meson (ρ), and isoscalar scalar meson (σ) fields, respectively. The counterterms ensure renormalizability. Since the meson fields are treated as C numbers, the coupled Euler-Lagrange equations of motion can be solved.[1] The parameters M, g_σ, g_ω, g_ρ, m_σ, m_ω, and m_ρ are treated as phenomenological constants.[1] The masses of the vector mesons (m_ω, m_ρ) are taken from experiment. The saturation properties of nuclear matter (density and binding energy/nucleon) are used to determine the ratios of the coupling constants to the masses for the σ meson $(g_\sigma/m_\sigma)^2$ and the ω meson $(g_\omega/m_\omega)^2$. The mass of the scalar isoscalar meson is obtained from fitting the surface thickness or rms radius of a finite nucleus such as ^{40}Ca. The ratio g_ρ/m_ρ is obtained by fitting the bulk symmetry energy/nucleon. We note for $N=Z$ nuclei, such as the present ^{16}O ground-state application the ρ meson does not contribute in the Hartree approximation for the orbitals. The parameters adopted in this study are listed in Table I.

The Euler Lagrange equations of motion yield a set of coupled equations which are solved in the Hartree approximation for spherical nuclei to obtain the desired orbitals. The equation obtained for the nucleon field is of the Dirac type, and for $N=Z$ nuclei of good parity is of the form

$$[i\gamma_\mu\partial^\mu - g_\omega\gamma^0 V_0(r) - e\tfrac{1}{2}(1+\tau_3)\gamma^0 A_0(r) - (M - g_\sigma\phi_0(r)]\psi(x) = 0 , \quad (9)$$

where $r = |\mathbf{x}|$.

The Dirac-Hartree wave functions and single-nucleon Hartree energies (ϵ_p, ϵ_h) are the stationary single-particle solutions and energy eigenvalues obtained by solving Eq.

TABLE I. Parameters used in particle-hole interactions denoted QHD-I and QHD-II in the text.[a]

	Parameter	Value
Couplings	g_σ^2	109.626
	g_ω^2	190.431
	g_ρ^2	65.226
	g_π^2	180.956
Masses	m_σ	520 MeV
	m_ω	783 MeV
	m_ρ	770 MeV
	m_π	138 MeV
	M	939 MeV

[a]See Ref. 3.

(9) consistently with the associated mean-field equations for the meson fields. The Dirac-Hartree single-particle wave functions used in this investigation were generated by the computer code HPLUS2C.[8] Particle-hole states of good isospin were desired so the Coulomb interaction was, in fact, turned off in generating the single-particle wave functions. The neutron and proton wave functions for a given orbit are therefore identical as are the corresponding single-particle energies.[9] The code HPLUS2C first solves for the core wave functions and then checks for self-consistency by attempting to generate spherically symmetric self-consistent potentials (mean fields). After the self-consistent core has been generated, the valence orbitals are solved for in the presence of the earlier determined core. Thus there is the usual assumption that the presence of the valence nucleon does not appreciably polarize the core. This does not appear to be a particularly good approximation for $T=0$ particle-hole excitations and a "backflow" correction term is needed in such studies.[5] Therefore we constrain our transition studies to $T=1$ particle-hole excitations where, due to the properties of the ρNN coupling the correction term should be small. Backflow corrections due to the pion may be important and are an area of future investigation.

The Dirac-Hartree wave functions obtained are those of a single Dirac particle in a central, parity-conserving field. These functions are eigenstates of J^2, S^2, T^2, J_z, and T_z and may be written

$$\psi_{njmt}(\mathbf{r})=\begin{bmatrix} i[G_{nljt}(r)/r]\Phi_{lm} \\ -[F_{nljt}(r)/r]\Phi_{\bar{l}m} \end{bmatrix}\eta_t \ . \tag{10}$$

In Eq. (10), the spin-orbit wave functions Φ_{lm} are expressed in terms of the spherical harmonics Y_{lm_l} and the two-component Pauli spinors χ_{m_s} as

$$\Phi_{lm}=\sum_{m_l m_s}\langle m_l \tfrac{1}{2} m_s | l \tfrac{1}{2} jm\rangle Y_{lm_l}(\Omega_r)\chi_{m_s} \ , \tag{11}$$

where it should be noted that the order of coupling in the Clebsch-Gordan coefficient is $(ls)j$, that is,

$$\mathbf{j}=\mathbf{l}+\mathbf{s} \ . \tag{12}$$

Furthermore, since ψ is not an eigenstate of $\mathcal{L}^2$ but is an eigenstate of the parity operator, $\bar{l}$ differs from l by one:

$$\bar{l}=l\pm 1, \quad \text{whenever } j=l\pm\tfrac{1}{2} \ . \tag{13}$$

The two-component isospinor η_t enters multiplicatively in Eq. (10). The radial wave functions corresponding to the upper (large) and lower (small) components are G and F, respectively.

Note, from Eq. (9), it is natural to define an effective nucleon mass $M^*(r)$ via

$$M^*(r)=M-g_\sigma\phi_0(r) \ . \tag{14}$$

Because the effective scalar potential $g_\sigma\phi_0$ is quite deep ($\sim$400 MeV) in the interior of the nucleus, the effective mass can be substantially reduced from the free nucleon mass value ($M^*\sim 0.6M$ near $r=0$). This allows considerable enhancement of the lower components of the Dirac orbitals compared to a free Dirac particle. This enhancement of the lower components could result in increased transition amplitudes for transition operators that connect upper and lower components. This effect has been the subject of considerable previous discussion and it is natural to speculate that the observation of particular enhanced transition rates would provide experimental evidence for the deep potential obtained in the present relativistic theories. We shall see in Sec. III that the situation is more complex and , that for the reactions studied in this investigation, some transitions resulting from coupling upper and lower components are actually reduced in the present calculations.

An important difference between the present Dirac-Hartree wave functions and those of, for example, a harmonic oscillator potential, apart from the four-component structure, is that the possibility exists for the Hartree calculation to produce an unbound valence orbital. This possibility is, in fact, realized in the case of the $d_{3/2}$ orbital of ^{16}O, which is actually unbound in nature. This $d_{3/2}$ orbital will therefore lie in the continuum. A continuum orbital such as the $d_{3/2}$ wave function in ^{16}O can be handled by discretizing the continuum. We carry out the Hartree calculation inside a sphere of radius 12 fm and require that the upper component radial wave functions [the $G(r)$] of the Dirac spinor solutions vanish at the boundary. This is the method followed by Furnstahl[10] who has also systematically studied collective excitations arising from various particle-hole bases incorporating continuum Hartree wave functions. As one increases the size of the aforementioned sphere, the density of orbitals with positive energies increases. Although the convergence of this procedure deserves further examination, we adopt Furnstahl's method[10] and suggest that refinements (i.e., using a larger sphere) be a subject for further study. In fact, our bases A and C (see below) will correspond to bases A and C used by Furnstahl.[10]

In what follows, bases A and B will consist of hole states taken from the $1p3/2$ and $1p1/2$ orbitals and particle states from the (bound) $1d5/3$ and $2s1/2$ valence orbitals as well as the lowest $1d3/2$ orbital in the discretized Hartree continuum. This corresponds closely to the usual "$1-\hbar\omega$" truncated basis often adopted in previous nonrelativistic calculations.

For basis A we use the calculated Hartree single-particle binding energies and, for comparison, in basis B we adopt binding energies obtained from neighboring nuclei with one more or one less neutron.

In basis C, we include the particle and hole states in

basis A plus additional particle states from the $d3/2$, $d5/2$, and $s1/2$ orbitals in the discretized continuum that result in unperturbed particle-hole configuration energies below 50 MeV. For this basis the calculated Hartree single-particle energies are used to obtain the unperturbed particle-hole configuration energies. A summary of the orbitals included and the associated single-particle energies for each basis is given in Table II.

C. Yukawa-Dirac particle-hole interactions

1. QHD-I interaction

Previous investigators[2,3] have denoted a specialized form of the quantum hydrodynamics (QHD) Lagrangian that contains only σ and ω meson couplings as QHD-I. An N-N interaction naturally resulting from the QHD-I Lagrangian contains terms arising only from the exchange of σ and ω mesons. Thus we have utilized an isospin-independent interaction containing Lorentz scalar and vector terms of the form

$$V(1,2)=-\frac{g_\sigma^2}{4\pi}\frac{e^{-m_\sigma r_{12}}}{r_{12}}+\frac{g_\omega^2}{4\pi}\frac{e^{-m_\omega r_{12}}}{r_{12}}\gamma^\mu(1)\gamma_\mu(2)\ , \tag{15}$$

where $r_{12}=|\mathbf{r}_1-\mathbf{r}_2|$. The couplings and masses adopted are listed in Table I.

2. QHD-II interactions

The QHD-II interaction includes πNN and ρNN couplings in the meson-nucleon Lagrangian.[2,3] Since one can couple the πNN vertices with either pseudoscalar (γ_5) or pseudovector ($\not{q}\gamma_5$) coupling, which are inequivalent in the many-body environment, we shall consider each coupling separately.

(i) Pseudoscalar coupling of pions to nucleon—QHD-II (PS). For the case of pseudo scalar coupling the form of the N-N interaction is given by

$$\begin{aligned}V(1,2)=&-\frac{g_\sigma^2}{4\pi}\frac{e^{-m_\sigma r_{12}}}{r_{12}}+\frac{g_\omega^2}{4\pi}\frac{e^{-m_\omega r_{12}}}{r_{12}}\gamma^\mu(1)\gamma_\mu(2)\\&+\frac{g_\pi^2}{4\pi}\frac{e^{-m_\pi r_{12}}}{r_{12}}\gamma^5(1)\gamma_5(2)\boldsymbol{\tau}_1\cdot\boldsymbol{\tau}_2\\&+\frac{g_\rho^2}{4\pi}\frac{e^{-m_\rho r_{12}}}{r_{12}}\gamma^\mu(1)\gamma_\mu(2)\frac{\boldsymbol{\tau}_1\cdot\boldsymbol{\tau}_2}{4}\ ,\end{aligned} \tag{16}$$

where τ is the usual nucleon Pauli isospin operator.

(ii) Pseudovector coupling of pions to nucleons—QHD-II (PV). Starting from a $\not{q}\gamma_5$ coupling, one can use the generalized Dirac equation [now containing an effective mass $M^*(r)$, see Eq. (14)] to eliminate derivatives in favor of the γ_5 coupling renormalized by the factor $M^*(r_1)M^*(r_2)/M^2$. Thus we obtain

$$\begin{aligned}V(1,2)=&-\frac{g_\sigma^2}{4\pi}\frac{e^{-m_\sigma r_{12}}}{r_{12}}+\frac{g_\omega}{4\pi}\frac{e^{-m_\omega r_{12}}}{r_{12}}\gamma^\mu(1)\gamma_\mu(2)\\&+\frac{g_\pi^2}{4\pi}\frac{M^*(r_1)}{M}\frac{M^*(r_2)}{M}\frac{e^{-m_\pi r_{12}}}{r_{12}}\gamma^5(1)\gamma_5(2)\boldsymbol{\tau}_1\cdot\boldsymbol{\tau}_2\\&+\frac{g_\rho^2}{4\pi}\frac{e^{-m_\rho r_{12}}}{r_{12}}\gamma^\mu(1)\gamma_\mu(2)\frac{\boldsymbol{\tau}_1\cdot\boldsymbol{\tau}_2}{4}\ .\end{aligned} \tag{17}$$

The couplings and masses adopted for the QHD-II interactions are given in Table I. A detailed discussion of the techniques used to solve Eqs. (4a) and (4b) using the interactions given above is contained in Ref. 9 and is available from the authors upon request.

D. Formulas for evaluating electroweak nuclear reactions

In Sec. III we present results for the nuclear linear response to electron scattering, muon capture, and beta

TABLE II. Single-particle orbitals included and energies for bases A, B, and C.

Basis A		Basis B		Basis C	
Orbital	Single particle energy	Orbital	Single particle energy[a]	Orbital	Single particle energy
			Particles		
				$4d3/2$	28.56
				$5s1/2$	26.95
				$4d5/2$	25.93
				$3d3/2$	15.93
				$4s1/2$	14.01
				$3d5/2$	13.89
				$2d3/2$	6.71
				$2d5/2$	5.29
				$3s1/2$	4.62
$1d3/2$	2.63	$1d3/2$	0.98	$1d3/2$	2.63
$2s1/2$	−1.21	$2s1/2$	−3.28	$2s1/2$	−1.21
$1d5/2$	−3.38	$1d5/2$	−4.14	$1d5/2$	−3.38
			Holes		
$1p1/2$	−12.49	$1p1/2$	−15.67	$1p1/2$	−12.49
$1p3/2$	−20.77	$1p3/2$	−21.83	$1p3/2$	−20.77

[a]See Ref. 13.

decay using the wave functions obtained from using the procedures discussed in the first part of the present section. For completeness, we briefly summarize the main formulas used to calculate these reactions. Some of the detailed forms for the appropriate transition operators are given in the Appendix.

E. Inelastic electron scattering

For this process, the nuclear ground state is linked to the nuclear excited states considered in the particle-hole model by the one-body electromagnetic operator, $\hat{J}^{\mu}(x)$,

$$\hat{J}^{\mu}(x)=\hat{\bar{\psi}}(x)\gamma^{\mu}Q\hat{\psi}(x)+\partial_{\nu}\left[\hat{\bar{\psi}}(x)\frac{\lambda}{2M}\sigma^{\mu\nu}\hat{\psi}(x)\right], \tag{18}$$

where the $\hat{\psi}(x)$ are baryon Heisenberg field operators. The nuclear current density adopted includes contributions from the anomalous magnetic moment λ,

$$\lambda=\lambda_p\tfrac{1}{2}(1+\tau_3)+\lambda_n\tfrac{1}{2}(1-\tau_3), \tag{19}$$

where λ_p (λ_n) is the proton (neutron) magnetic moment and M is the nucleon mass. The operator Q projects out protons:

$$Q=\tfrac{1}{2}(1+\tau_3). \tag{20}$$

The Feynman diagram for inelastic electron scattering by one-photon exchange is depicted in Fig. 1(a), where the four momentum transferred from the nucleus is q_{μ}. The differential cross-section for inelastic electron scattering in the plane-wave Born approximation is written[11]

$$\frac{d\sigma}{d\Omega}=4\pi\sigma_M[1+(2\epsilon\sin^2(\theta/2)/M_{\text{target}})]^{-1}F^2,$$

where

$$F^2=\left[\frac{q_{\mu}^2}{q^2}\right]^2F_L^2+\left[\frac{1}{2}\left[-\frac{q_{\mu}^2}{q^2}\right]+\tan^2(\theta/2)\right]F_T^2$$

$$F_L^2=(2J_i+1)^{-1}\sum_{J=0}^{\infty}|\langle J_f\|\hat{M}_J(q)\|J_i\rangle|^2$$

$$F_T^2=(2J_i+1)^{-1}\sum_{J=1}^{\infty}[|\langle J_f\|\hat{T}^{el}_J(q)\|J_i\rangle|^2+|\langle J_f\|\hat{T}^{\text{mag}}_J(q)\|J_i\rangle|^2]. \tag{21}$$

In Eq. (21), ϵ is the incident energy of the electron, θ is the scattering angle and M_{target} is the mass of the target. Using the metric of Bjorken and Drell,[12] the four-momentum transfer squared is

$$q_{\mu}^2=q_0^2-\mathbf{q}^2, \tag{22}$$

where

$$q_0=E_i-E_f, \tag{23}$$

and E_i (E_f) is the initial (final) nuclear target energy. The Mott cross-section σ_M is given by

$$\sigma_M=[\alpha\cos(\theta/2)/2\epsilon\sin^2(\theta/2)]^2, \tag{24}$$

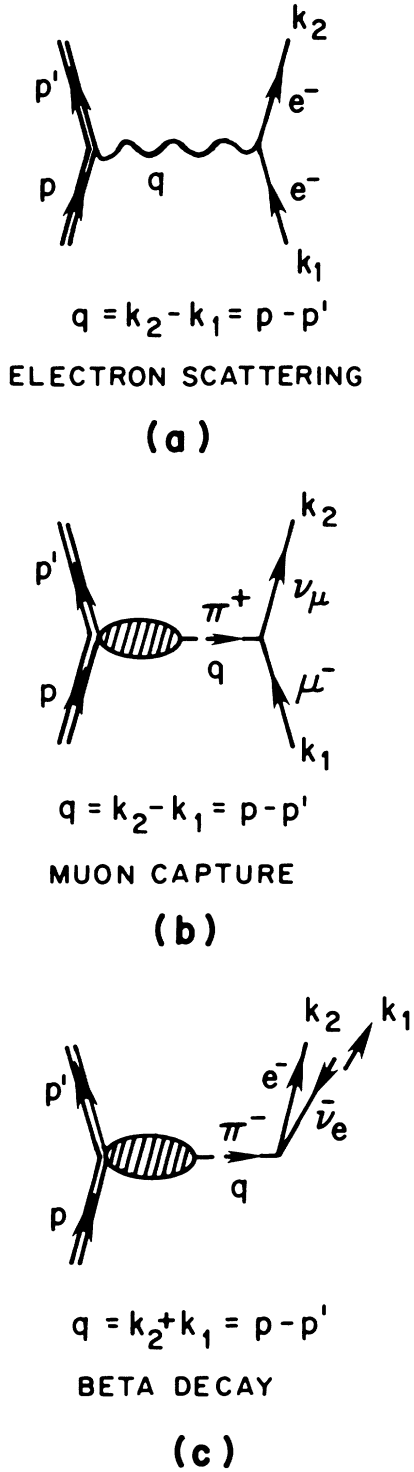

FIG. 1. Definition of four momenta for (a) electron scattering (b) muon capture (pionic contribution to axial current shown) and (c) beta decay (pionic contribution to axial current shown).

where α is the fine structure constant. In Eq. (21), the reduced matrix elements are given by Eq. (7) (note here we suppress isospin factors and subscripts), where the first-quantized multipole transition operators are specified in the Appendix.

Using the transition operators defined above we have

calculated squared form-factors for inelastic electron scattering to selected $T=1$ excited states in ^{16}O. In order to compare with previous nonrelativistic calculations and experiment, we plot and discuss in the next section,

$$\tilde{F}^2(q)=\frac{F^2(q)}{[1+\tan^2(\theta/2)]} , \tag{25}$$

where $F^2(q)$ is defined in Eq. (21). We also include in the calculated form factors the single-nucleon form factors squared,[11,13]

$$f^2_{SN}(q^2_\mu)=[1-q^2_\mu/q^2_N]^{-4} , \tag{26}$$

where

$$q_N=855 \text{ MeV}/c , \tag{27}$$

and the center-of-mass correction factors,[11,13]

$$g^2_{CM}(q^2)=e^{2y/A} , \tag{28}$$

where

$$y=(\tfrac{1}{2}bq)^2 . \tag{29}$$

In Eq. (28), A is the atomic mass number and in Eq. (29), b is the oscillator parameter used in a nonrelativistic shell model. We use the value $b=1.77F$ for ^{16}O.

F. Muon capture

We will study, in Sec. III, muon capture rates resulting from the capture of a $1s$ Bohr orbital muon by an ^{16}O nucleus. This process is depicted in Fig. 1(b), where the leptonic weak current is coupled to the weak nuclear current, $J^{(-)}_\mu(x)$:

$$\hat{J}^{(-)}_\mu(x)=\hat{J}^{(-)}_\mu(x)+\hat{J}^{(-)}_{\mu 5}(x) . \tag{30}$$

In Eq. (30), $\hat{J}^{(-)}_\mu(x)$ is the charge-changing weak vector current (see the Appendix for details):

$$\hat{J}^{(-)}_\mu(x)=\hat{\bar{\psi}}(x)\gamma_\mu\tau_-\hat{\psi}(x)+\partial^\nu\left[\hat{\bar{\psi}}(x)\frac{\lambda}{2M}\sigma_{\mu\nu}\hat{\psi}(x)\right] , \tag{31}$$

where $\lambda\equiv(\lambda_p-\lambda_n)\tau_-$. The second term in Eq. (30) is the weak axial-vector current $\hat{J}^{(-)}_{\mu 5}(x)$ described in the Appendix.

Figure 1(b) exhibits the induced pionic contribution to the total axial-vector current. Since the nucleon can be coupled to the pion with either pseudoscalar (γ_5) or pseudovector $\not{q}\gamma_5$ coupling, we employ currents based on both methods of coupling (see Appendix). For the case of pseudoscalar coupling, the strength [see Eq. (A22)]

$$F_P(q^2_\mu)=\frac{2M^*(x)}{m^2_\pi-q^2_\mu} \tag{32}$$

is the analog of the nonrelativistic result[14]

$$F_P(q^2_\mu)=\frac{2M}{m^2_\pi-q^2_\mu} , \tag{33}$$

where Eq. (32) is obtained by assuming pion-pole dominance and using the Dirac equation for the Dirac-Hartree spinors:

$$[i\partial\!\!\!/-g_v\gamma^0V_0(x)-M^*(x)]\psi(x)=0 . \tag{34}$$

The muon capture rate is given by the formula,[14]

$$\omega_{fi}=\frac{G^2\nu^2}{2\pi}|\phi_{1s}|^2_{\text{av}}\frac{4\pi}{2J_i+1}\left[\sum_{J=0}^{\infty}|\langle J_f\|\hat{M}_J(\nu)-\hat{\mathcal{L}}_j(\nu)\|J_i\rangle|^2+\sum_{J\geq 1}|\langle J_f\|\hat{T}^{\text{mag}}_J(\nu)-\hat{T}^{\text{el}}_J(\nu)\|J_i\rangle|^2\right] . \tag{35}$$

In Eq. (35), G is the Fermi coupling constant and ν is the momentum of the outgoing neutrino. The rate above includes the square modulus of the muon wave function. Since the muon in Fig. 1(b) is treated in the limit $k_1/\epsilon_1\to 0$, this is a nonrelativistic wave function computed for a point charge and evaluated at the origin. The finite extent of the nucleus is included by multiplying by the standard reduction factor.[14] The rate above is also multiplied by a phase-space factor,

$$(1+\nu/M_{\text{target}})^{-1} . \tag{36}$$

The multipole operators in Eq. (35) are defined in terms of the current in Eq. (30) as follows:

$$\hat{M}_{JM}(q)\equiv\hat{M}_{JM}+\hat{M}^5_{JM}=\int d\mathbf{x}[j_J(qx)Y_{JM}(\Omega_x)]\hat{J}^0(x) , \tag{37}$$

$$\hat{\mathcal{L}}_{JM}(q)\equiv\hat{L}_{JM}+\hat{L}^5_{JM}=\frac{i}{q}\int d\mathbf{x}\{\nabla[j_J(qx)Y_{JM}(\Omega_x)]\}\cdot\hat{\mathbf{J}}(x) , \tag{38}$$

$$\hat{T}^{\text{el}}_{JM}(q)\equiv\hat{T}^{\text{el}}_{JM}(q)+\hat{T}^{\text{el5}}_{JM}(q)=\frac{1}{q}\int d\mathbf{x}[\nabla x j_J(qx)\mathbf{Y}^M_{JJ1}(\Omega_x)]\cdot\hat{\mathbf{J}}(x) , \tag{39}$$

$$\hat{T}^{\text{mag}}_{JM}(q)\equiv\hat{T}^{\text{mag}}_{JM}(q)+\hat{T}^{\text{mag5}}_{JM}(q)=\int d\mathbf{x}j_J(qx)\mathbf{Y}^M_{JJ1}\cdot\mathbf{J}(x) . \tag{40}$$

The operators in each term above are defined in the Appendix.

G. Beta decay

We will present results, in Sec. III, for the beta decay of the first excited 0^- state in ^{16}N to the 0^+ (g.s.) of ^{16}O. This state is found experimentally to have an excitation energy of $E_x=0.120$ MeV relative to the ^{16}N (g.s.) Thus, including the mass difference, $M(^{16}\text{N})-M(^{16}\text{O})=10.51$ MeV, this state should lie at $E_x=10.63$ MeV above the ^{16}O(g.s.) The general diagram for the beta-decay process is shown in Fig. 1(c). Defining k_μ as the electron four momentum and ν as

the three momentum of the neutrino, the three-momentum transfer $\mathbf{q}$ from the nucleus is

$$\mathbf{q}=\mathbf{k}+\boldsymbol{\nu} . \tag{41}$$

We denote the electron energy by ϵ and define β as

$$\boldsymbol{\beta}\equiv\frac{\mathbf{k}}{\epsilon} . \tag{42}$$

For $0^-\rightarrow 0^+$ beta-decay transitions, the rate is given by[14]

$$d\omega=\frac{G^2}{2\pi^3}k\epsilon(W_0-\epsilon)^2 d\epsilon\frac{d\Omega_k}{4\pi}\frac{d\Omega_\nu}{4\pi}4\pi\{(1+\hat{\boldsymbol{\nu}}\cdot\boldsymbol{\beta})|\langle 0^+\|\hat{M}^5_0(q)\|0^-\rangle|^2+[1-\hat{\boldsymbol{\nu}}\cdot\boldsymbol{\beta}+2(\hat{\boldsymbol{\nu}}\cdot\hat{\mathbf{q}})(\hat{\mathbf{q}}\cdot\hat{\boldsymbol{\beta}})]|\langle 0^+\|\hat{L}^5_0(q)\|0^-\rangle|^2$$
$$-\hat{\mathbf{q}}\cdot(\hat{\boldsymbol{\nu}}+\boldsymbol{\beta})2\,\mathrm{Re}\langle 0^+\|\hat{L}^5_0(q)\|0^-\rangle\langle 0^+\|\hat{M}^5_0(q)\|0^-\rangle^*\}2\pi\eta/[\exp(2\pi\eta)-1] . \tag{43}$$

This expression must be integrated over the electron energy ϵ from the electron rest mass to W_0, the maximum electron energy. Neglecting the recoil of the nucleus, W_0 is taken as the excitation energy of the excited state relative to the 0^+(g.s.) The wave function of the outgoing electron in the beta-decay process will be enhanced by the Coulomb interaction of the electron with the daughter nucleus ^{16}O. If one uses Coulomb wave functions in the matrix element of the weak interaction the analysis is very complicated. Instead we follow an approach similar to that in muon capture of multiplying by a factor[14]

$$F(Z,e)\simeq|\phi^0_k(0)_c/\phi_k(0)|^2=2\pi\eta/(\exp 2\pi\eta-1) , \tag{44}$$

where $\eta\equiv ZZ'\alpha/\beta$ with $Z=8$ for ^{16}O and $Z'=-1$ for β^- decay. The factor $F(Z,e)$ above is the square modulus of the ration of the Coulomb wave function computed for a point charge Z to a plane wave evaluated at the origin.

In order to facilitate the integrations over the angles in Eq. (43), we follow the traditional method of making long-wavelength reductions of the transition operators (the limit $q\rightarrow 0$). These reductions are listed in the Appendix [see Eqs. (A47)–(A50)].

III. RESULTS AND DISCUSSION

A. Spectrum of ^{16}O excited states

We have used the procedures and input discussed in the preceding section to obtain the spectrum of selected $T=0$ and $T=1$ states for ^{16}O. More specifically we have solved the set of coupled equations given by Eqs. (4a) and (4b) using as input the Yukawa-Dirac interactions given by Eqs. (15), (16), and (17). The single-particle orbitals are obtained from Dirac-Hartree calculations using a Lagrangian containing $NN\sigma$ and $NN\omega$ interactions. For a closed shell $N=Z$ nucleus, contributions from the isovector ρ and π mesons vanish in the Hartree mean-field approximation used to obtain the Hartree orbitals. The coupling and mass input parameters used in the calculations are listed in Table I. Single-particle and hole energies were either obtained from the results of the Hartree calculations or from neighboring nuclei (see Table II).

Representative results of the calculations are shown in Figs. 2–5. Furnstahl[10] has previously reported the results of RPA calculations in a relativistic model. In what follows we briefly summarize some previous conclusions as well as some new results shown in Figs. 2–5. The calculation of Furnstahl[10] used Hartree single-particle energies and allowed selected continuum single-particle orbitals (for example, basis A and C of the present calculations). Our results are consistent with Furnstahl's for the same set of input and basis states. This provides an independent check of some of the computer codes used to generate wave functions in the present calculations. Furnstahl[10] has noted previously that the pure particle-hole energies obtained are within a couple of MeV of those obtained by using the masses of neighboring nuclei. This can be seen from Table II or from the first spectrum (labeled unperturbed) shown in Fig. 2 where Hartree energies are denoted by solid lines and the energies obtained phenomenologically from using the masses of neighboring nuclei are shown as dashed lines. Overall the main feature is a greater spread in the pure Hartree spectrum compared to the pure phenomenological spectrum. Turning on the particle-hole interactions results in the

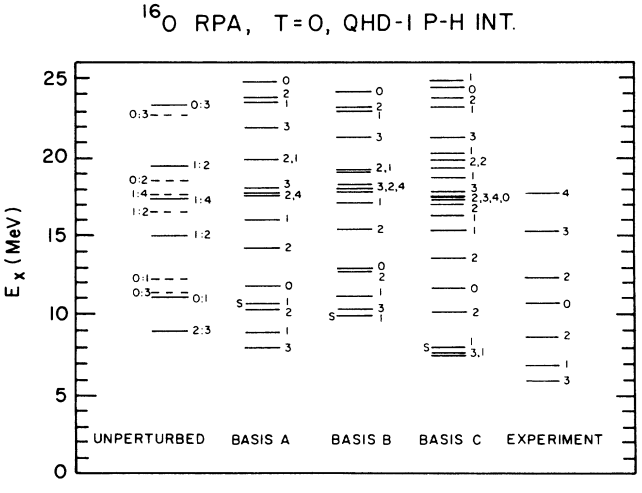

FIG. 2. Negative parity, $T=0$, RPA, excited-state energy levels calculated using the QHD-I residual interaction and various bases described in the text. The unperturbed levels obtained from Hartree single-particle energies (neighboring nuclei) are shown as solid (dashed) lines. The spurious 1^- levels are indicated by an S.

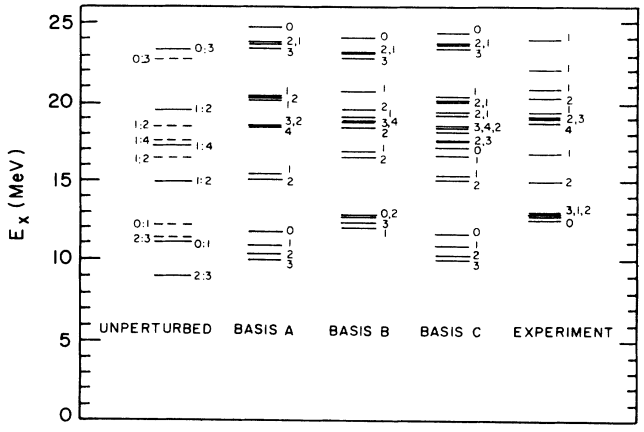

FIG. 3. Same as Fig. 2 except $T=1$ negative parity levels are shown.

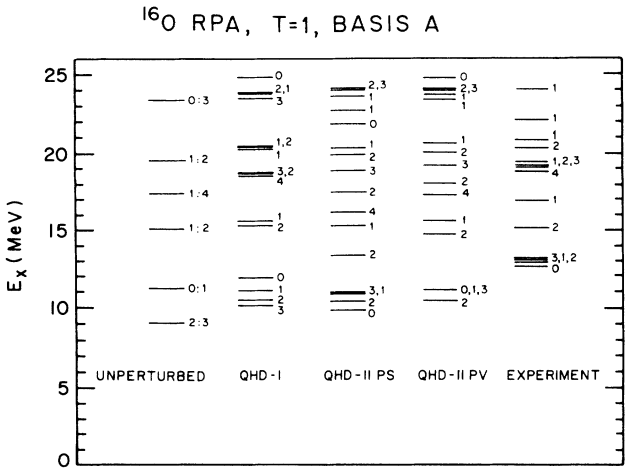

FIG. 5. Same as Fig. 4 except $T=1$ negative parity levels are shown.

mixing of pure particle-hole basis states resulting in level diagrams such as those shown in Figs. 2–5. It has been previously noted[10] that in the relativistic model the contributions to the particle-hole interaction coming from each meson exchange separately can be quite large. However, due to cancellations among the individual meson exchange contributions the total particle-hole interaction results in matrix elements similar to those obtained in nonrelativistic calculations. Furnstahl[10] has previously noted (using basis C) that using the QHD-II interaction, including π and ρ meson exchange, results in a particle-hole interaction that apparently pushes down unnatural parity (pionlike) states too far in energy. This is particularly noticeable for the QHD-II (PS) interaction. The fact that pseudovector coupling tends to damp the strong effective pion exchange interaction obtained in QHD-II (PS) is the reason that the QHD-II (PV) interaction yields unnatural parity states closer to the experimental levels identified with these particle-hole states. Thus, QHD-II (PV) is apparently preferred on the basis

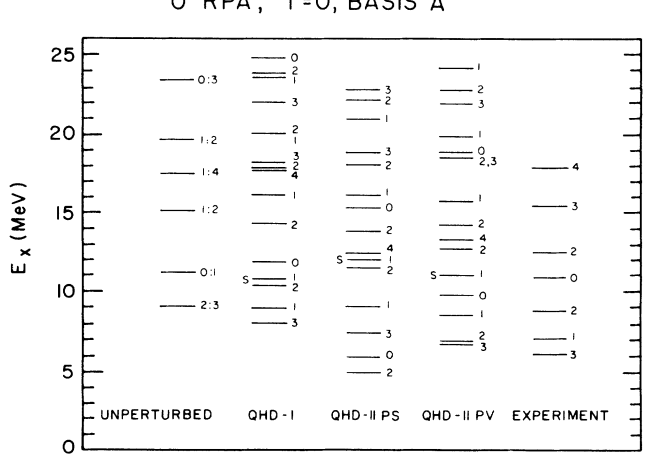

FIG. 4. Negative parity $T=0$, RPA, excited-state energy levels using the QHD-I or QHD-II residual interaction and basis A.

of this phenomenology. These conclusions are based on using basis C.

We can use the results shown in Figs. 2–5 to study the effects of using the masses of neighboring nuclei to obtain the single-particle energies. This approximation has often been adopted in previous nonrelativistic calculations.[13] The adoption of phenomenological single-particle energies allows one to include effects other than those included in the Hartree mean-field approximation. Such effects might include multiparticle multihole configurations in the ^{16}O ground state, Fock terms, and, relatedly, single-pion exchange contributions to single-particle energies. Of course from a theoretical perspective such phenomenology has serious disadvantages associated with the resulting lack of a systematic procedure for including higher-order corrections.

If the QHD-I particle-hole interaction is adopted, one finds (see Figs. 1 and 3) that for A (Hartree energies and single unbound $1d_{3/2}$ orbital) the level diagram is quite similar to that obtained for basis C (Hartree energies and continuum basis). In fact, the main differences occur because the continuum calculation includes additional basis states. Figures 4 and 5 illustrate the results for basis A assuming different residual interactions. The qualitative trends are similar to those obtained for basis C by Furnstahl. In particular for $T=1$ states all three interactions studied result in the predicted energies of the lowest-lying quartet of states ($T=1$, $J^{\pi}=0^-,1^-,2^-,3^-$) being considerably lower than the corresponding experimental energies. Moreover, as in the case of basis C, one finds that for both $T=0$ and $T=1$ states the QHD-II interaction results in most unnatural parity state ($0^-,2^-,4^-$) energies being significantly lower than is observed experimentally.

The use of QHD-I and basis B (phenomenological single-particle energies and single unbound $1d_{3/2}$ orbital) allows the $T=1$ lowest-lying quartet to be closer to the observed experimental levels (see Fig. 3) although the ordering of the closely spaced levels is still not correctly given . On the other hand, for the $T=0$ lowest-lying levels the use of phenomenological single-particle energies

and QHD-I results in the predicted energies of the lowest levels being significantly higher than the predictions for basis *A* and *C* and is in disagreement with experiment (see Fig. 2).

B. Inelastic electron scattering form-factors for ^{16}O

Using the nuclear wave functions discussed above and the relativistic expressions for electron-nucleus scattering given by Eqs. (18)–(29) and in the Appendix, we have studied the nuclear linear response to electron scattering. Because of the inherent uncertainties in the energy level predictions ($\sim$1–2 MeV) and, in some cases, the intrinsic widths of the states involved, we have grouped the states in ^{16}O into complexes centered near 13, 17, and 19 MeV as well as one comprising the giant resonance region. There exists a previously published comparison between the experimental results for these complexes and a standard nonrelativistic [Tamm-Danoff approximation (TDA)] linear response theory.[13] The $T=0$ states were not included in the nonrelativistic theory and are not included in the *present* complexes since in each case they yield small calculated form factors and thus are predicted to be weakly excited.

Furnstahl[10] has previously reported a study of the distribution of dipole strength in ^{16}O in a relativistic model. He has also studied individual form factors such as those for the low-lying $T=0$ collective states in ^{16}O and several $T=1$ states for which experimental data is available. For some of the $T=1$ states of interest in this paper, his main conclusions are that (a) both the QHD-I and QHD-II interactions yield reasonable results for the energy distribution of dipole strength and (b) the magnitude of predicted form factors for states dominated by a single unperturbed particle-hole configuration are generally larger than the associated experimental form factors.

The states included in the various complexes for basis *A*, *B*, and *C* are listed in Table III. Admixture amplitudes and electron scattering form factors for individual states are available from the authors on request. We show representative results for the form-factor complexes using the QHD-I particle-hole interaction in Figs. 6 and 7.

1. The 13 and 17 MeV complexes

The quantity $\tilde{F}^2(q)$, defined by Eq. (25), for the 13 and 17 MeV complexes is plotted in Figs. 6(a)–(c) for basis *A*, *B*, and *C*, respectively. The points with error bars are the experimental data taken from Refs. 15 and 16. The solid curves are the present RPA results. The dashed curves are the nonrelativistic TDA results of Donnelly and Walker[13] obtained using harmonic oscillator wave functions and using phenomenological unperturbed configuration energies obtained from the masses of neighboring nuclei. Both theory and experiment in the case of the 13 MeV complex have been multiplied by 10 to allow for a simultaneous display with the 17 MeV complex.

The RPA results for the 13 MeV complex are essentially unchanged whether one uses the bases *A*, *B*, or *C*. The effect of including higher-lying continuum states in basis *C* is unobservable when compared to the basis *A* result. This is understandable since these low-lying $T=1$ states contain little particle-hole configuration mixing. The basis *B* curves shows less excitation than found from basis *A* for values of q less than 300 MeV/c. This is because the 2^- constituent (see Table III) is less strongly excited, for this range of momentum transfer, in basis *B*

TABLE III. The $T=1$ constituent states included in the 13, 17, and 19 MeV and giant resonance complexes [see Sec. III, (e,e')].

	RPA energy eigenvalue (MeV)			
	Basis *A*	Basis *B*	Basis *C*	Nonrelativistic TDA[a]
13 MeV				
1^-	11.14	12.24	11.11	14.38
2^-	10.56	12.95	10.51	13.59
3^-	10.22	12.62	10.20	13.57
17 MeV				
1^-	15.65	17.10	16.88	18.46
2^-	15.32	16.75	15.31	18.45
19 MeV				
1^-	20.21	19.20	20.16	20.73
2^-	18.61	18.58	18.26	19.77
2^-	20.29	19.68	20.24	20.96
3^-	18.67	18.98	18.64	19.17
4^-	18.59	18.89	18.58	19.86
Giant resonance				
1^-	20.47	20.79	20.45	23.26
1^-	23.82	23.19	23.76	26.13
2^-	23.86	23.23	23.81	24.28
3^-	23.56	22.92	23.56	25.30

[a]See Ref. 13.

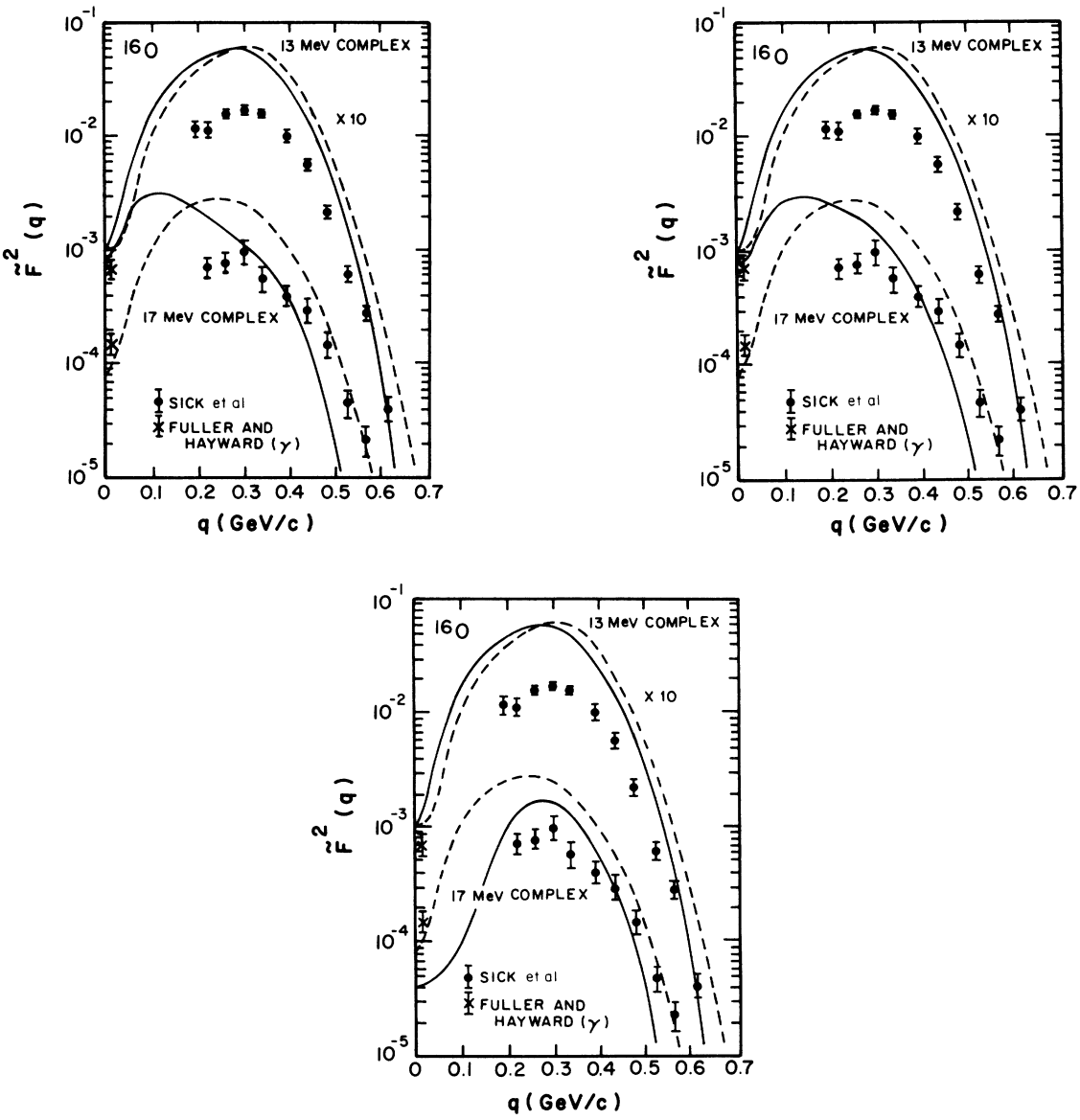

FIG. 6. (a) Electron scattering form factors for ^{16}O for the 13 and 17 MeV complexes. Theory and experiment have been multiplied by 10 for the 13 MeV complex. The solid line represents the relativistic calculation using basis A discussed in the text. The dashed line is a nonrelativistic calculation taken from Ref. 13. The experimental data denoted Sick *et al.* is from Ref. 15, and the data of Fuller and Hayward is from Ref. 16. (b) Same as (a) except basis B is used in the relativistic calculation. (c) Same as (a) except basis C is used in the relativistic calculation.

than in basis A. The result is a curve in basis B that more closely agrees with that from the nonrelativistic TDA calculation (which uses the same unperturbed energies as adopted in basis B). We note that in each basis the calculated form-factor squared, as in the nonrelativistic TDA case, is still roughly three times the experimental result. Since the 3^- constituent (see Table III) is less strongly excited (by approximately a factor of 2) for $q > 300$ MeV/c, than in the nonrelativistic TDA result,[13] the total form-factor squared in the present QHD-I calculators drops off more rapidly in this region of q. At the photon point ($q \approx 13$ MeV/c) the RPA curve is just outside (above) the range of experimental error. This is also the case for the nonrelativistic TDA prediction shown.

Using the 1^- and 2^- states produced by the RPA calculation in basis A and B leads to calculated squared form factors for the 17 MeV complex that fail to reproduce experiment. It is the 1^- state at 15.65 MeV in basis A and 17.10 MeV in basis B (see Table III) that peaks at low q that causes the difficulty. The excitation for these 1^- states is roughly three times that for the corresponding 1^- state found in the nonrelativistic TDA calculation. On the other hand, the 2^- state which peaks at about 200 MeV/c is about a factor of 3 smaller than the nonrelativistic TDA result for $q \gtrsim 200$ MeV/c. This gives better agreement with experiment in this region of q.

The situation is somewhat improved in the case where basis C is employed in the RPA structure calculation.

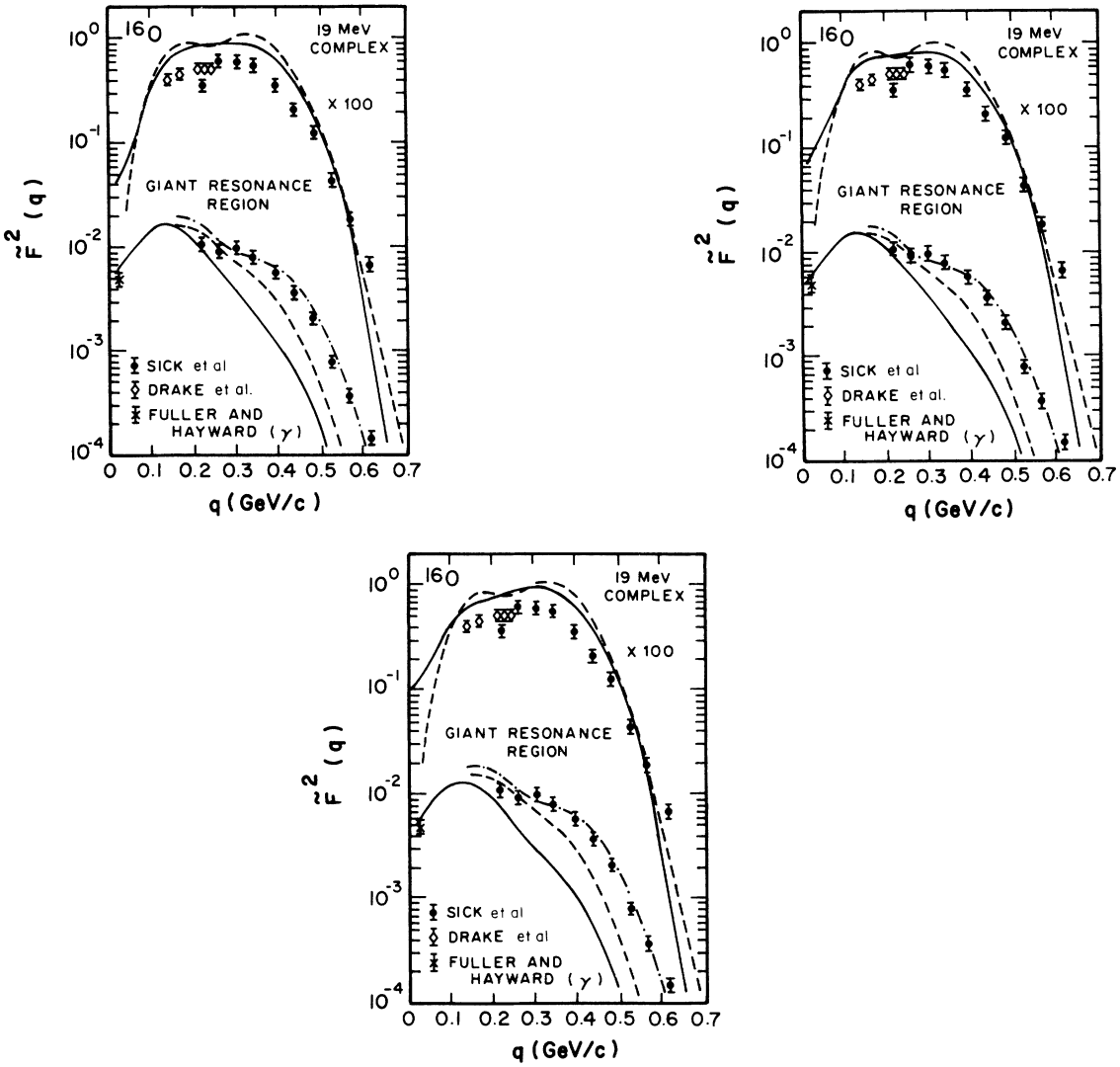

FIG. 7. (a) Same as Fig. 6(a) except the 19 MeV complex and the giant resonance regions are shown. The data denoted Drake *et al.* is from Ref. 17. Theory and experiment have been multiplied by 100 for the 19 MeV complex. The dot-dashed line is a nonrelativistic calculation including the quasielastic contribution calculation in Ref. 13. (b) Same as (a) except basis B is used in the relativistic calculation. (c) Same as (a) except basis C is used in the relativistic calculation.

Here we find that in addition to a 1^- state at 15.58 MeV there is a 1^- state at 16.88 MeV. The lower-lying state is mainly that found earlier in the smaller basis. If we only include the higher-lying state in the total form-factor squared for the 17 MeV complex we obtain the result shown in Fig. 6(c). Since the 2^- form factor from basis C is similar to that obtained in basis A and B, we see that the inclusion of this new 1^- state greatly improves the agreement at low q resulting in an overall agreement with experiment that is better than that found in the nonrelativistic TDA calculation. The nonrelativistic TDA curve requires a reduction factor of about 2 in order to attain the same level of excitation as the experimental data. At the same time, however, the basis C RPA curve misses the photon point ($q \approx 17$ MeV/c) by being about a factor of 4 too low. Of course, while the inclusion of this new 1^- state at 17 MeV improves the agreement with the experimental form factors in this energy region, one is now faced with the problem of a predicted strongly excited 1^- state at 15 MeV.

2. *The 19 MeV and giant resonance region complexes*

In Figs. 7(a)–(c) we show the total form factors squared for the 19 MeV and giant resonance complexes for bases $A-C$. The points carrying error bars are experimental data from Refs. 15–17. The solid curves are the RPA results of the present calculation while the dashed curve is the nonrelativistic TDA result of Donnelly and Walker.[13] The dot-dashed curve is the nonrelativistic TDA curve plus a nonrelativistic quasielastic contribution.[19] This curve is included only to provide a qualitative estimate of quasielastic contributions and should be ignored when making a comparison of relativistic and nonrelativistic results. The experimental data and the

theoretical curves in the 19 MeV complex have each been multiplied by 100 to allow for a simultaneous display of the giant resonance region complex.

Differences between the RPA curves of total form factors squared for basis A, B, and C are slight in the 19 MeV complex. The biggest of these occurs at low q, where the form factor for the 1^- state at the photon point is the least in basis A and the greatest in basis C. In this region of low q, all the relativistic RPA curves are consistently enhanced relative to the nonrelativistic TDA result. The 1^- state individual form factor exhibits a diffractive minimum at a q of about 240 MeV/c which becomes very sharply defined in basis C. This results in a better agreement with the data points in this region compared to the nonrelativistic calculation. In the region of high q, the form factors obtained by using basis A, B, and C are nearly identical and consistently below the nonrelativistic TDA curve. This occurs because the present calculations yield a smaller 4^- and 2^- (at 20.29 MeV) form factor than for the nonrelativistic calculations. The rise of the form factor seen in the nonrelativistic TDA calculation for q values in the region of 150 and 350 MeV/c are missing in the present RPA calculations. This is due in part to a less strongly excited lowest 2^- state in this complex. The relativistic calculation resolves approximately half of the discrepancy between the nonrelativistic TDA result and experiment in these regions of q.

The RPA form factors squared for transitions to the complex of states in the giant resonance region are nearly identical for basis A, B, and C. The curve obtained from basis C shows slightly less excitation strength for $q > 100$ MeV/c than found from basis A and B. In this region of q the agreement between the RPA curves and the experimental data is poor. However, since a relativistic estimate of the quasielastic contribution is not available, a direct comparison is difficult to make. On the other hand, comparison with the nonrelativistic TDA curve shows a large reduction in transition strength for $q \gtrsim 150$ MeV/c for the relativistic predictions compared to the nonrelativistic results. In each basis, the RPA, 3^- form factor squared is about a factor of 3 smaller than that from the nonrelativistic TDA calculation. At the same time, the agreement with the experimental photon point is excellent for each basis employed. Furnstahl has previously noted that the difference between relativistic RPA and relativistic TDA calculations is small for $T=1$ dipole states with the largest effect being a $\sim 20\%$ reduction for the most collective dipole state using a QHD-I particle-hole interaction.

We have investigated the source of the slight reduction between nonrelativistic TDA calculations and the present relativistic RPA calculations for the 4^- $T=1$ stretched state. We find that there is a slight reduction $\lesssim 10\%$ in going from the TDA to the RPA (independent of q and not a relativistic effect). This is consistent with earlier transition rate renormalization studies.[18] The relativistic and nonrelativistic TDA 4^- $T=1$ transition rates are quite similar between 300 and 400 MeV/c with the nonrelativistic rate being slightly larger ($\lesssim 10\%$) near 300 MeV/c and the relativistic rate being slightly larger ($\lesssim 20\%$) near 400 MeV/c. Note that oscillator orbitals were used for the nonrelativistic rates discussed above, while Hartree orbitals were adopted for the relativistic calculations. We regard the differences quoted above as small and conclude that the sensitivity (for both orbital and relativistic transition operator differences) of the 4^- $T=1$ stretched state transition rate is weak.

The situation for selected 3^- $T=1$ states can be quite different. For example we noted that the 3^- $T=1$ state in the giant resonance region complex is significantly weaker (approximately a factor of 3) in the present relativistic RPA calculations compared to a previous nonrelativistic TDA calculation. This state is almost completely a $1d_{3/2}\,(1p_{3/2})^{-1}$ particle-hole state in the present calculations. From earlier work we expect a small reduction in going from the TDA to the RPA.[18] We have examined the various contributions to the relativistic and nonrelativistic rates (Coulomb and electric multipoles, upper and lower component contribution) and find that the large reduction can be traced to a corresponding reduction of contributions coming from upper components only (for both the Coulomb and transverse electric multipoles) and thus is an apparently trivial effect arising from the use of an unbound $1d_{3/2}$ orbital in the present relativistic calculations and a bound oscillator $1d_{3/2}$ orbital in the nonrelativistic prediction taken from Ref. 13.

C. Weak interaction rates for ^{16}O

1. *Muon capture rates in ^{16}O*

There have been previous investigations concerning the influence of relativistic nuclear dynamics on predictions of muon capture and β-decay rates in nuclei. Previous research has indicated that calculated muon capture rates and beta-decay rates in the $^{16}\mathrm{O}(0^+\leftrightarrow 0^-)^{16}\mathrm{N}$ transition are significantly enhanced due to the presence of M^* in the Dirac equation and in the weak nuclear current.[19,20] When M^* effects are not included, the ratio of $0^+\leftrightarrow 0^-$ partial rates for muon capture to those for beta decay are outside the range of experiment (about a factor of 2 too large). On the other hand, when M^* effects are schematically included the rates are apparently significantly enhanced. In this latter case, while both the predicted muon capture rates and the beta-decay rates appear to be at variance with experiment, the ratio of their rates is inside the range of experiment.[20]

One interesting question is whether these enhancements of the weak $^{16}\mathrm{O}(0^+\rightarrow 0^-)^{16}\mathrm{N}$ transition rates persist in a more complete relativistic treatment using (a) Dirac-Hartree single-nucleon wave functions (containing implicit M^* effects), (b) the configuration admixtures obtained from relativistic nuclear structure calculations for the excited states reported at the beginning of this section, and (c) the full Lorentz structure of the relativistic weak transition operators. In addition, one would like to compare the muon capture rates to the 0^-, 1^-, and 2^- $T=1$ states in ^{16}N to those obtained in nonrelativistic calculations. The remainder of this subsection is devoted to a discussion of the calculated muon capture rates. The beta-decay rate predictions are discussed in Sec. III C 2.

In Table IV we show capture rates to the 0^-, 1^-, and

TABLE IV. RPA total muon capture rates $(s^{-1})\times 10^2$. PS and PV refer to the πNN coupling assumed in the weak axial current. The same πNN coupling has been assumed in QHD-II as in the weak axial current. Values in parentheses are TDA rates.

	Basis *A*		Basis *B*		Basis *C*		Nonrelativistic
	PS	PV	PS	PV	PS	PV	TDA[a]
0^-							
QHD-I	68	86	68	87	86	112	(115)
QHD-II	102	98	101	98	(139)	176	
1^-							
QHD-I	451	451	450	450	534	534	(596)
QHD-II	408	406	408	405	(563)	450	
2^-							
QHD-I	548	465	528	448	548	465	(505)
QHD-II	626	499	597	477	(619)	508	
Total							
QHD-I	1067	1003	1047	984	1168	1111	(1215)
QHD-II	1136	1002	1106	980	(1321)	1134	

[a]See Ref. 21.

2^- states of ^{16}N that are below 30 MeV based on calculations adopting different particle-hole interactions, bases, and forms for the weak axial current. The states above 30 MeV carry only a small amount of the total transition strength as do the higher spin 3^- and 4^- states.

The rates shown are for nuclear structure calculations adopting the RPA. We have also carried out similar calculations using the TDA. We find that if one assumes a QHD-I interaction and either PS or PV weak axial coupling, the RPA *total* rate to a given type (J^π) of state is *smaller* ($\lesssim 10\%$) than the TDA rates. On the other hand, the RPA total rate to 0^- states is significantly *larger* ($\lesssim 40\%$) than the TDA rate for QHD-II PV and PS, for each basis employed. The RPA total rate to 2^- states is slightly enhanced ($\lesssim 4\%$) relative to the TDA rate for QHD-II (PS) using basis *A* and *B*. RPA and TDA rates can be considerably different for *individual* transitions as well (see $0^+ \leftrightarrow 0^-$ discussion below). From Table IV one observes that the 0^- and 1^- predictions using basis *B* are not significantly different from those obtained using basis *A*. Even for the 2^- predictions for basis *B* and basis *A* the difference is $\lesssim 5\%$. For 0^- and 2^- states PV and PS predictions can be significantly different (for the same basis and particle-hole interaction). The total capture rate is somewhat less sensitive to the assumption of PS or PV coupling in the weak axial current, yielding differences on the order of 12 percent. There is not an appreciable difference between nonrelativistic TDA predictions and relativistic TDA *total* capture rates obtained using the present procedure. As an example we note that a nonrelativistic TDA prediction for the capture rate[21] yields $\Lambda_\mu = 122\times 10^3\ s^{-1}$, while we find using the relativistic approach and basis *C* the TDA predictions (not shown in Table IV) are (a) QHD-I, PV: $120\times 10^3\ s^1$, (b) QHD-II, PS: $132\times 10^3\ s^{-1}$, and (c) QHD-II, PV: $117\times 10^3\ s^{-1}$. The RPA and TDA predictions should be compared with the experimental results $(97\pm 5)\times 10^3\ s^{-1}$ (Ref. 22) and $(98\pm 3)\times 10^3\ s^{-1}$ (Ref. 23).

While we obtain no significant difference between nonrelativistic and relativistic TDA *total* rates (certainly no large enhancement of the relativistic rates), there can be significant differences between PS and PV predictions and between relativistic and nonrelativistic predictions for rates to a given state. In order to investigate the origin of such differences it is useful to examine partial rates in more detail. We show, in Table V, the partial muon capture rates for capture leading from the 0^+ ground state of ^{16}O to the lowest 0^- state of ^{16}N. The RPA results show that the PS predictions are generally lower than PV predictions for a given particle-hole interaction with predictions based on a QHD-I interaction being lower than those obtained using the QHD-II particle-hole interaction. For comparative purposes we note that the nonrelativistic TDA rate[21] is 1825 s^{-1} and the experimental rate[24] is 1110–1560 s^{-1}. Thus the results for QHD-I adopting PS coupling in the weak axial current are closer to the experimental results, while the other predictions are significantly higher than experiment and are larger than the nonrelativistic TDA predictions. Since some of the discrepancy between theory and experiment is probably attributable to multiparticle, multihole configurations[18] in the ground state (beyond those consistent with the RPA approximation) and exchange current contributions it is not possible to motivate a particular coupling (PS or PV) based on a simple comparison between present theory and experiment. We further discuss this point in the conclusions section.

The nonrelativistic TDA predictions are most appropriately compared with relativistic TDA calculations. Thus we show in Table VI the relativistic TDA results. Note that the lowest $0^+ \rightarrow 0^-$ transition PV predictions are substantially larger than the PS results with the particular NR relativistic TDA prediction quoted lying between the PS and PV results. For the total rate the relativistic TDA PV rate is lower than the PS rate (for basis *B* and QHD-I) and both are reduced compared to the nonrelativistic TDA prediction (see Table VI).

It is of interest to determine the origin of the large differences occurring in the lowest $0^+ \rightarrow 0^-$ partial rate predictions. There are three potential contributors to the

TABLE V. RPA muon capture and beta-decay partial rates (s^{-1}) for the ^{16}O (g.s.) ($\leftrightarrow$) ^{16}N (0^-) transition.

	Basis *A*		Basis *B*		Basis *C*		Nonrelativistic
	PS	PV	PS	PV	PS	PV	TDA[a]
Λ_μ							1825
QHD-I	1492	2260	1424	2172	1262	1924	
QHD-II	2712	2863	2511	2748		3557	
Λ_β							0.3
QHD-I	0.376	0.318	0.363	0.306	0.308	0.259	
QHD-II	0.691	0.422	0.648	0.407		0.555	
$(\Lambda_\mu/\Lambda_\beta)\times 10^{-3}$							6.0
QHD-I	4.0	7.1	3.9	7.1	4.1	7.4	
QHD-II	3.9	6.8	3.9	6.7		6.4	

[a]See Ref. 21 for Λ_μ; Λ_β calculated by the present authors.

differences: (a) relativistic Dirac single-particle orbitals, (b) admixture coefficients associated with different particle-hole interactions [i.e., QHD-I, QHD-II (PS,PV)] and assumed pure configuration particle-hole energies (i.e., the difference between basis *A* and basis *B*), and (c) the form assumed for the weak axial nuclear current (PS or PV coupling). The differences that can be attributed to the effect of adoption of different configuration energies is small as can be seen by comparing corresponding entries (i.e., same residual interaction and assumed weak current) of basis *A* with those of basis *B*. The Dirac orbitals used in basis *A* are identical to those of basis *B*. Obviously there can be very significant differences attributed to which residual interaction is used. For example, see Table V, and see the differences between QHD-I and QHD-II for a given basis and assumed (PS or PV) coupling in the weak axial current. This difference arises solely from the different admixture coefficients for linear combinations of particle-hole states induced by different residual interactions. We find that for a given basis and type of residual interaction there is significant difference in the predicted rate between assuming PS and PV coupling in the weak axial transition operator with the PV predictions being higher than the corresponding PS predictions. We show, in Table VII, the TDA muon capture rate for the ^{16}O (g.s.)$\rightarrow$ ^{16}N (0^-) transition for the lowest 0^-, $T=1$ excited state of ^{16}N. The results indicate that for the QHD-I interaction (for all bases and PV or PS coupling) the relativistic TDA and RPA (see Table V) predictions are quite similar, with the RPA results being slightly larger. For the QHD-II interaction the relativistic RPA rate is significantly higher than the corresponding relativistic TDA rate.

2. *Beta-decay rates in ^{16}N ($0^-\rightarrow 0^+$) ^{16}O transitions*

The results for the beta decay of the first excited 0^- state of ^{16}N to the 0^+ (g.s.) of ^{16}O are summarized in

TABLE VI. Partial muon capture rates in (s^{-1}) to the 0^-, 1^-, and 2^- ($T=1$) states of ^{16}O calculated in the TDA using basis *B* and QHD-I.

J^π	E_x (MeV)	PS	PV	Nonrelativistic DTA[a]	Experimental range
0^-	13.08	1401	2137	1835	1100–1560[b]
	24.17	5466	6562	9629	
1^-	12.24	2770	2770	2772	1400–1850[b]
	17.13	9846	9846	5808	
	19.20	3443	3443	3060	
	20.89	20 668	20 668	20 114	
	23.21	11 771	11 771	27 879	
2^-	12.97	21 604	19 326	13 261	
	16.75	207	293	8	
	18.59	3978	2022	1765	
	19.70	27 860	23 332	26 843	
	23.23	2 515	1614	8594	
Total partial rate		111 529	104 784	121 516	97 000±5000[c] 98 000±3000[d]

[a]See Ref. 21.
[b]See Ref. 24.
[c]See Ref. 22.
[d]See Ref. 23.

TABLE VII. TDA muon capture and beta-decay partial rates (s^{-1}) for the ^{16}O (g.s.) ($\leftrightarrow$) ^{16}N (0^-) transition.

	Basis					
	A		*B*		*C*	
	PS	PV	PS	PV	PS	PV
Λ_μ						
QHD-I	1466	2221	1401	2137	1198	1831
QHD-II	1414	2314	1335	2243	959	2125
Λ_β						
QHD-I	0.369	0.313	0.357	0.302	0.291	0.244
QHD-II	0.346	0.329	0.329	0.321	0.226	0.293

Table V. For PS or PV coupling and QHD-I we note the absence of significant enhancements in the beta-decay rate relative to the nonrelativistic result for all the bases considered. There are significant enhancements if the QHD-II residual interaction and PS coupling is adopted. As will be discussed in the final section we place more significance on the PV coupling results and thus the enhancement obtained for QHD-II, PV, basis *C* is noteworthy. The relativistic TDA beta-decay predictions are shown in Table VII. Note that in the relativistic TDA there are no significant enhancements in the beta-decay rate compared to the nonrelativistic prediction. The theoretical predictions should be compared with the experimental result[25] $\Lambda_\beta = 0.43 \pm 0.10\ s^{-1}$.

Thus depending on the details of the relativistic calculation there may or may not be significant enhancements compared to a nonrelativistic calculation. Earlier work[19] that suggested enhancements would naturally occur differs from the present calculation in that we use relativistic Hartree orbitals, configuration mixed wave functions obtained using a relativistic form for the residual interaction, and a fully relativistic treatment of the relevant transition operators [involving nontrivial $M^*(r)$ effects].

IV. DISCUSSION AND CONCLUSIONS

The purpose of this work was to apply a relativistic theory of nuclei to a study of the isovector electroweak nuclear response. The random-phase approximation (RPA) to linear response theory was used to study inelastic electron scattering, muon capture, and beta decay on the mass 16 system. While it is of interest to compare the results with experiment, perhaps a more meaningful comparison is with standard nonrelativistic calculations of a similar degree of sophistication. For example, adoption of the RPA means that a significant truncation of shell-model basis has occurred and thus form factors and decay rates—calculated either relativistically or nonrelativistically—may not agree with experiment for the trivial reason that for a particular transition a "particle-hole" model is inadequate for obtaining the nuclear transition density.

Certain of the weak interaction capture and decay rates and nuclear excited state energy levels calculated using QHD-II were sensitive to whether PS or PV coupling was used for the πNN vertex. Generally, for nuclear energy levels, PS coupling tends to excessively lower the energies of non-normal parity isovector states. For weak interactions the form of the weak axial current adopted preserves partial conservation of axial-vector current (PCAC) in the nuclear environment only if PV coupling is adopted (for PS coupling, terms involving the derivative of the effective mass violate PCAC).

The inelastic electron scattering predictions suggest that the overall isovector response of *complexes* is not qualitatively different than those found using a nonrelativistic model. Individual states may have somewhat different form factors (see Sec. III). The stretched 4^-, $T=1$ state, while somewhat reduced compared to nonrelativistic calculations, is still too strongly excited compared to experimental results. This is probably associated with the truncation of the basis and not a problem with the model of the nuclear dynamics.

The total muon capture rate on ^{16}O is not very sensitive to the type of coupling or residual interaction adopted. The results are similar to those obtained in a nonrelativistic model and exceed the experimental results by 10–30%.

Partial weak interaction rates can be extremely sensitive to the assumption of PS or PV coupling and the residual interaction adopted. Of particular significance are the axial transitions $0^+ \leftrightarrow 0^-$ studied for muon capture and beta decay. These transitions are of special interest because they involve the time component of the weak axial current for which exchange current contributions may be especially important.[26,27] The sensitivity of these partial rates to effects studied herein cannot be fully exploited without additional theoretical research. The areas we regard as important for future investigation include (a) satisfactory incorporation of pions in a relativistic model involving chiral symmetry and, relatedly, an elucidation of the relation between the pion and the sigma meson already present in the current relativistic models, (b) utilization of a larger shell model basis including both conventional multiparticle multihole states as well as nucleon-antinucleon states (incorporating as an example vacuum polarization effects), and (c) calculations of meson exchange current, and relatedly, isobar effects in a consistent model assuming relativistic dynamics.

This work was supported in part by a National Science Foundation Grant PHY86-06364.

APPENDIX

For completeness we summarize below the relativistic forms for the transition operators used in the electron

scattering, muon capture, and beta-decay reactions studied in the main text.

1. Vector current operators

The explicit forms for the relativistic electroweak vector current transition operators are listed below. These operators are associated with the conserved electromagnetic vector current or the conserved charge-changing weak vector current. The general form of the vector current is

$$\hat{J}^{\mu}(x)=\hat{\bar{\psi}}(x)\gamma^{\mu}Q\hat{\psi}(x)+\partial_{\nu}\left[\hat{\bar{\psi}}(x)\frac{\lambda}{2M}\sigma^{\mu\nu}\hat{\psi}(x)\right], \tag{A1}$$

where the $\hat{\psi}(x)$ are the baryon Heisenberg field operators and

$$Q=\begin{cases}\frac{1}{2}(1+\tau_3), & \text{vector current}\\ \tau_{\pm}, & \text{charge-changing weak vector current},\end{cases} \tag{A2}$$

$$\lambda=\begin{cases}\lambda_p\frac{1}{2}(1+\tau_3)+\lambda_n\frac{1}{2}(1-\tau_3), & \text{vector current}\\ (\lambda_p-\lambda_n)\tau_{\pm}, & \text{charge-changing weak vector current}.\end{cases} \tag{A3}$$

In Eq. (A1), M is the nucleon mass and in Eq. (A3), λ_p (λ_n) is the proton (neutron) magnetic moment. The multipole transition operators appearing in the text are expressed in terms of the $J^{\mu}(x)$ in Eq. (A1) by

$$\hat{L}_{JM}(q)=\frac{i}{q}\int d\mathbf{x}\{\nabla[j_J(qx)Y_{JM}(\Omega_x)]\}\cdot\mathbf{J}(x), \tag{A4}$$

$$\hat{M}_{Jm}(q)=\int d\mathbf{x}\, j_J(qx)Y_{JM}(\Omega_x)\hat{J}^0(x), \tag{A5}$$

$$\hat{T}^{\rm el}_{JM}(q)=\frac{1}{q}\int d\mathbf{x}[\nabla\times j_J(qx)\mathbf{Y}^M_{JJ1}(\Omega_x)]\cdot\mathbf{J}(x), \tag{A6}$$

$$\hat{T}^{\rm mag}_{JM}(q)=\int d\mathbf{x}\, j_J(qx)\mathbf{Y}^M_{JJ1}(\Omega_x)\cdot\mathbf{J}(x), \tag{A7}$$

where, using a standard notation

$$M^M_J(q\mathbf{x})\equiv j_J(qx)Y^M_J(\Omega_x), \tag{A8}$$

$$\mathbf{M}^M_{JL}(q\mathbf{x})\equiv j_L(qx)\mathbf{Y}^M_{JL1}(\Omega_x), \tag{A9}$$

and where $j_J(qx)$ is a spherical Bessel function, $Y^M_J(\Omega_x)$ is a spherical harmonic, and $\mathbf{Y}^M_{JL1}(\Omega_x)$ is a vector spherical harmonic defined via

$$\mathbf{Y}^M_{JL1}(\Omega_x)=\sum_{m\lambda}\langle Lm\,1\lambda|(L\,1)JM\rangle Y^m_L(\Omega_x)\hat{\mathbf{e}}_{\lambda}, \tag{A10}$$

with

$$\hat{\mathbf{e}}_{\pm1}=\mp(\hat{\mathbf{e}}_x\pm i\hat{\mathbf{e}}_y)/2^{1/2}, \tag{A11}$$

$$\hat{\mathbf{e}}_0=\hat{\mathbf{e}}_z. \tag{A12}$$

Using the continuity equation and integration by parts, one can show that matrix elements of $\hat{L}_{JM}(q)$ can be expressed in terms of those of $\hat{M}_{JM}(q)$:

$$\langle J_f\|\hat{L}_J\|J_i\rangle=\frac{q^0}{q}\langle J_f\|\hat{M}_J\|J_i\rangle. \tag{A13}$$

The transition operators have the following matrix structure in the space of the nucleon Dirac-Hartree four component spinors using the gamma matrices of Ref. 12:

$$M_{JM}(q)=\begin{bmatrix}QM^M_J(q\mathbf{x}) & -i\lambda' q\Sigma''^M_J(q\mathbf{x})\\ i\lambda' q\Sigma''^M_J(q\mathbf{x}) & QM^M_J(q\mathbf{x})\end{bmatrix}, \tag{A14}$$

$$T^{\rm el}_{JM}(q)=\begin{bmatrix}q\lambda'\Sigma^M_J(q\mathbf{x}) & i(Q-\lambda'^0_q)\Sigma'^M_J(q\mathbf{x})\\ i(Q+\lambda' q^0)\Sigma'^M_J(q\mathbf{x}) & -q\lambda'\Sigma^M_J(q\mathbf{x})\end{bmatrix}, \tag{A15}$$

$$T^{\rm mag}_{JM}(q)=\begin{bmatrix}iq\lambda'\Sigma'^M_J(q\mathbf{x}) & (Q-\lambda' q^0)\Sigma^M_J(q\mathbf{x})\\ (Q+\lambda' q^0)\Sigma^M_J(q\mathbf{x}) & -iq\lambda'\Sigma'^M_j(q\mathbf{x})\end{bmatrix}, \tag{A16}$$

where $\lambda'=\lambda/2M$. The two-component matrix operators Σ^M_J, Σ'^M_J, and Σ''^M_J are defined via

$$\Sigma^M_J(q\mathbf{x})\equiv\mathbf{M}^M_J(q\mathbf{x})\cdot\boldsymbol{\sigma}, \tag{A17}$$

$$\Sigma'^M_J(q\mathbf{x})\equiv -i\left[\frac{1}{q}\nabla\times\mathbf{M}^M_{JJ}(q\mathbf{x})\right]\cdot\boldsymbol{\sigma}=[J]^{-1}[-J^{1/2}\mathbf{M}^M_{JJ+1}(q\mathbf{x})+(J+1)^{1/2}\mathbf{M}^M_{JJ-1}(q\mathbf{x})]\cdot\boldsymbol{\sigma}, \tag{A18}$$

$$\Sigma''^M_J(q\mathbf{x})\equiv\left[\frac{1}{q}\nabla M^M_J(q\mathbf{x})\right]\cdot\boldsymbol{\sigma}=[J]^{-1}[(J+1)^{1/2}\mathbf{M}^M_{JJ+1}(q\mathbf{x})+J^{1/2}\mathbf{M}^M_{JJ-1}(q\mathbf{x})]\cdot\boldsymbol{\sigma}, \tag{A19}$$

where σ is the usual Pauli two-component spin operator. The reduced matrix elements of the above operators are found using the general results:

$$\langle n'(l'\tfrac{1}{2})j'\|M_J(q\mathbf{x})\|n(l\tfrac{1}{2})j\rangle=\frac{1}{\sqrt{(4\pi)}}(-)^{J+j+1/2}[l'][l][j'][j][J]\begin{Bmatrix} l' & j' & \frac{1}{2} \\ j & l & J \end{Bmatrix}\begin{bmatrix} l' & J & l \\ 0 & 0 & 0 \end{bmatrix}\langle n'l'j'|j_J(qx)|nlj\rangle \ , \tag{A20}$$

$$\langle n'(l'\tfrac{1}{2})j'\|\mathbf{M}_{JL}(q\mathbf{x})\cdot\boldsymbol{\sigma}\|n(l\tfrac{1}{2})j\rangle=\frac{1}{\sqrt{(4\pi)}}(-)^{l'}6^{1/2}[l'][l][j'][j][L][J]\begin{Bmatrix} l' & l & L \\ \frac{1}{2} & \frac{1}{2} & 1 \\ j' & j & J \end{Bmatrix}\begin{bmatrix} l' & L & l \\ 0 & 0 & 0 \end{bmatrix}\langle n'l'j'|j_L(qx)|nlj\rangle \ . \tag{A21}$$

2. Axial vector current operators

The relativistic transition operators resulting from the charge-changing, weak axial-vector current are listed below. Since this current contains an induced coupling to the π meson, we list both pseudoscalar and pseudovector couplings for this contribution.

a. Pseudoscalar coupling

For pseudoscalar πNN coupling the axial-vector current is written

$$\hat{J}^{(\pm)}_{\mu 5}(x)=\hat{\bar{\psi}}(x)\gamma_\mu\gamma_5 w^{(\pm)}\hat{\psi}(x)-\frac{2M^*(x)q_\mu}{m_\pi^2-q_\mu^2}\hat{\bar{\psi}}(x)\gamma_5 w^{(\pm)}\hat{\psi}(x) \ , \tag{A22}$$

where,

$$q_\mu\equiv(p-p')_\mu \ , \tag{A23}$$

$$M^*(x)\equiv\text{nucleon effective mass} \ , \tag{A24}$$

$$m_\pi\equiv\text{pion mass} \ , \tag{A25}$$

$$w^{(\pm)}=-1.23\tau_\pm, \quad \tau_\pm=\tfrac{1}{2}(\tau_x\pm i\tau_y) \ . \tag{A26}$$

The gamma matrices used are those of Ref. 12. In matrix form, one has

$$\hat{J}^{(\pm)}_{05}(x)=\hat{\psi}^\dagger(x)\begin{bmatrix} 0 & -\dfrac{2M^*(x)q_0}{m_\pi^2-q_\mu^2}+1 \\ \dfrac{2M^*(x)q_0}{m_\pi^2-q_\mu^2}+1 & 0 \end{bmatrix}w^{(\pm)}\hat{\psi}(x) \tag{A27}$$

and

$$\hat{\mathbf{J}}^{(\pm)}_5(x)=\hat{\psi}^\dagger(x)\begin{bmatrix} \boldsymbol{\sigma} & -\dfrac{2M^*(x)}{m_\pi^2-q_\mu^2}\mathbf{q} \\ \dfrac{2m^*(x)}{m_\pi^2-q_\mu^2}\mathbf{q} & \boldsymbol{\sigma} \end{bmatrix}w^{(\pm)}\hat{\psi}(x) \ . \tag{A28}$$

We list below the matrix structure of the new operators appearing in Eqs. (37)–(40) of the main text associated with the axial vector current. The following operators should each be multiplied by the isospin factor, $w^{(\pm)}$:

$$M^5_{JM}(q)=\begin{bmatrix} 0 & \left[1-\dfrac{2M^*(x)q^0}{m_\pi^2-q_\mu^2}\right]M^M_J(q\mathbf{x}) \\ \left[1+\dfrac{2M^*(x)q^0}{m_\pi^2-q_\mu^2}\right]M^M_J(q\mathbf{x}) & 0 \end{bmatrix}, \tag{A29}$$

$$L^5_{JM}(q)=\begin{bmatrix} i\Sigma''^M_J(q\mathbf{x}) & -\dfrac{2}{m_\pi^2-q_\mu^2}[qM^*(x)M^M_J(q\mathbf{x})-M^{*'}(x)\Xi'^M_J(q\mathbf{x})] \\ \dfrac{2}{m_\pi^2-q_\mu^2}[qM^*(x)M^M_J(q\mathbf{x})-M^{*'}(x)\Xi''^M_J(q\mathbf{x})] & i\Sigma''^M_J(q\mathbf{x}) \end{bmatrix}, \tag{A30}$$

$$T^{\mathrm{el}5}_{JM}(q)=\begin{bmatrix} i\Sigma'^M_J(q\mathbf{x}) & \dfrac{2M^{*'}(x)}{m_\pi^2-q_\mu^2}\Xi'^M_J(q\mathbf{x}) \\ -\dfrac{2M^{*'}(x)}{m_\pi^2-q_\mu^2}\Xi'^M_J(q\mathbf{x}) & i\Sigma'^M_J(q\mathbf{x}) \end{bmatrix}, \tag{A31}$$

$$T^{\mathrm{mag}5}_{JM}(q)=\begin{bmatrix} \Sigma^M_J(q\mathbf{x}) & 0 \\ 0 & \Sigma^M_J(q\mathbf{x}) \end{bmatrix}, \tag{A32}$$

where

$$M^{*'}(x)\equiv\frac{dM^*(x)}{dx}\ . \tag{A33}$$

The quantities M^M_J, $\mathbf{M}^M_{JL}$, Σ^M_J, Σ'^M_J, and Σ''^M_J have been defined above in Eqs. (A8), (A9), (A17), (A18), and (A19), respectively. For the off-diagonal contributions of Eqs. (A30) and (A31) involving the derivatives of $M^*(x)$, one needs to define projections of expression (A9) onto the unit vector $\hat{\mathbf{x}}$:

$$\begin{aligned}\mathbf{M}^M_{JL}(q\mathbf{x})\cdot\hat{\mathbf{x}}&=(-)^J[L]\begin{bmatrix} L & 1 & J \\ 0 & 0 & 0 \end{bmatrix}j_L(qx)Y_{JM}(\Omega_x),\quad L=J\pm1\\ &=0,\quad L=J\ .\end{aligned} \tag{A34}$$

We obtain

$$\begin{aligned}\Xi^M_J(q\mathbf{x})&\equiv\mathbf{M}^M_{JJ}(q\mathbf{x})\cdot\hat{\mathbf{x}}\\ &=0\ ,\end{aligned} \tag{A35}$$

$$\Xi'^M_J(q\mathbf{x})\equiv-i\left[\frac{i}{q}\nabla\times\mathbf{M}^M_{JJ}(q\mathbf{x})\right]\cdot\hat{\mathbf{x}}=[J]^{-1}[-J^{1/2}\mathbf{M}^M_{JJ+1}(q\mathbf{x})+(J+1)^{1/2}\mathbf{M}^M_{JJ-1}(q\mathbf{x})]\cdot\hat{\mathbf{x}}\ , \tag{A36}$$

and

$$\Xi''^M_J(q\mathbf{x})\equiv\left[\frac{1}{q}\nabla M^M_J(q\mathbf{x})\right]\cdot\hat{\mathbf{x}}=[J]^{-1}[(J+1)^{1/2}\mathbf{M}^M_{JJ+1}(q\mathbf{x})+J^{1/2}\mathbf{M}^M_{JJ-1}(q\mathbf{x})]\cdot\hat{\mathbf{x}}\ . \tag{A37}$$

b. Pseudovector coupling

For pseudovector πNN coupling the form of the axial-vector current may be written

$$\hat{J}^{(\pm)}_{\mu5}(x)=\hat{\bar{\psi}}(x)\gamma_\mu\gamma_5 w^{(\pm)}\hat{\psi}(x)+\frac{q_\mu}{m_\pi^2-q_\mu^2}\hat{\bar{\psi}}(x)\not{q}\gamma_5 w^{(\pm)}\hat{\psi}(x)\ . \tag{A38}$$

The quantities appearing in Eq. (A38) are defined following (A22). In matrix form,

$$\hat{J}^{(\pm)}_{05}(x)=\hat{\psi}^{\dagger}(x)\begin{bmatrix} \dfrac{-q_0(\mathbf{q}\cdot\boldsymbol{\sigma})}{m_\pi^2-q_\mu^2} & \dfrac{q_0^2}{m_\pi^2-q_\mu^2}+1 \\ \dfrac{q_0^2}{m_\pi^2-q_\mu^2}+1 & \dfrac{-q_0(\mathbf{q}\cdot\boldsymbol{\sigma})}{m_\pi^2-q_\mu^2} \end{bmatrix} w^{(\pm)}\hat{\psi}(x)\ , \tag{A39}$$

$$\mathbf{J}^{(\pm)}_{5}(x)=\hat{\psi}\,\dagger(x)\begin{bmatrix} \boldsymbol{\sigma}-\dfrac{(\mathbf{q}\cdot\boldsymbol{\sigma})}{m_\pi^2-q_\mu^2}\mathbf{q} & \dfrac{q_0}{m_\pi^2-q_\mu^2}\mathbf{q} \\ \dfrac{q_0}{m_\pi^2-q_\mu^2}\mathbf{q} & \boldsymbol{\sigma}-\dfrac{(\mathbf{q}\cdot\boldsymbol{\sigma})}{m_\pi^2-q_\mu^2}\mathbf{q} \end{bmatrix} w^{(\pm)}\hat{\psi}(x)\ . \tag{A40}$$

By eliminating $\mathbf{q}$, as in the previous case of pseudoscalar coupling we find the following matrix structure associated with the various operators

$$M^5_{JM}(q)=\begin{bmatrix} -\dfrac{iq_0q}{m_\pi^2-q_\mu^2}\Sigma''^M_J(q\mathbf{x}) & \left[\dfrac{q_0^2}{m_\pi^2-q_\mu^2}+1\right]M^M_J(q\mathbf{x}) \\ \left[\dfrac{q_0^2}{m_\mu^2-q_\mu^2}+1\right]M^M_J(q\mathbf{x}) & -\dfrac{iq_0q}{m_\pi^2-q_\mu^2}\Sigma''^M_J(q\mathbf{x}) \end{bmatrix}, \tag{A41}$$

$$L^5_{JM}(q)=\begin{bmatrix} \left[1-\dfrac{q^2}{m_\pi^2-q_\mu^2}\right]i\Sigma J''^M(q\mathbf{x}) & \left[\dfrac{q_0q}{m_\pi^2-q_\mu^2}\right]M^M_J(q\mathbf{x}) \\ \left[\dfrac{q_0q}{m_\pi^2-q_\mu^2}\right]M^M_J(q\mathbf{x}) & \left[1-\dfrac{q^2}{m_\pi^2-q_\mu^2}\right]i\Sigma''^M_J(q\mathbf{x}) \end{bmatrix}, \tag{A42}$$

$$T^{\mathrm{el}5}_{JM}(q)=\begin{bmatrix} i\Sigma'^M_J(q\mathbf{x}) & 0 \\ 0 & i\Sigma'^M_J(q\mathbf{x}) \end{bmatrix}, \tag{A43}$$

$$T^{\mathrm{mag}5}_{JM}(q)=\begin{bmatrix} \Sigma^M_J(q\mathbf{x}) & 0 \\ 0 & \Sigma^M_J(q\mathbf{x}) \end{bmatrix}. \tag{A44}$$

It is interesting to note that Eqs. (A31) and (A44) are identical, i.e., $T^{\mathrm{mag}5}_{JM}(q)$ is the same for both pseudoscalar and pseudovector coupling. With the following parity assignments,

$$(-)^J\text{:}\ \ \hat{M}_{JM},\hat{L}_{JM},\hat{T}^{\mathrm{el}}_{JM},\hat{T}^{\mathrm{mag}5}_{JM}\ , \tag{A45}$$

$$(-)^{J+1}\text{:}\ \ \hat{T}^{\mathrm{mag}}_{JM},\hat{M}^{5}_{JM},\hat{L}^{5}_{JM},\hat{T}^{\mathrm{el}5}_{JM}\ , \tag{A46}$$

one concludes that natural-parity transitions that proceed by $\hat{T}^{\mathrm{mag}5}_{JM}$ will have the same rate for both pseudoscalar and pseudovector coupling.

To calculate beta-decay rates for $0^-\rightarrow 0^+$ transitions we utilize the long-wavelength reductions (the limit $q\rightarrow 0$) of the operators $M^5_{00}(q)$ and $L^5_{00}(q)$:

(a) pseudoscalar coupling,

$$M^5_{00}(0)\underset{(q\rightarrow 0)}{\rightarrow}\begin{bmatrix} 0 & \left[-\dfrac{2M^*(x)q^0}{m_\pi^2-q_0^2}+1\right]Y_{00}(\Omega_x) \\ \left[\dfrac{2M^*(x)q^0}{m_\pi^2-q_0^2}+1\right]Y_{00}(\Omega_x) & 0 \end{bmatrix}, \tag{A47}$$

$$L^5_{00}(q)\underset{(q\rightarrow 0)}{\rightarrow}\frac{q}{3}\begin{bmatrix} ix\mathbf{Y}^0_{011}(\Omega_x)\cdot\boldsymbol{\sigma} & -\dfrac{2[xM^{*'}(x)+3M^*(x)]}{m_\pi^2-q_0^2}Y_{00}(\Omega_x) \\ \dfrac{2[xM^{*'}(x)+3M^*(x)]}{m_\pi^2-q_0^2}Y_{00}(\Omega_x) & ix\mathbf{Y}^0_{011}(\Omega_x)\cdot\boldsymbol{\sigma} \end{bmatrix}, \tag{A48}$$

and (b) pseudovector coupling

$$M^5_{00}(q) \underset{(q\to 0)}{\to} \begin{bmatrix} 0 & \left[\frac{q_0^2}{m_\pi^2 - q_0^2}+1\right] Y_{00}(\Omega_x) \\ \left[\frac{q_0^2}{m_\pi^2 - q_0^2}+1\right] Y_{00}(\Omega_x) & 0 \end{bmatrix}, \tag{A49}$$

$$L^5_{00}(q) \underset{(q\to 0)}{\to} \frac{q}{3} \begin{bmatrix} i\mathbf{x}\,\mathbf{Y}^0_{011}(\Omega_x)\cdot\boldsymbol{\sigma} & \left[\frac{3q_0}{m_\pi^2 - q_0^2}\right] Y_{00}(\Omega_x) \\ \left[\frac{3q_0}{m_\pi^2 - q_0^2}\right] Y_{00}(\Omega_x) & i\mathbf{x}\,\mathbf{Y}^0_{011}(\Omega_x)\cdot\boldsymbol{\sigma} \end{bmatrix}. \tag{A50}$$

*Present address: Center for Naval Analyses, 4401 Ford Avenue, Alexandria, VA 22302.

[1]L. D. Miller and A. E. S. Green, Phys. Rev. C **5**, 241 (1972); L. D. Miller, *ibid.* **9**, 537 (1974); **12**, 710 (1975); R. Brockmann and W. Weise, *ibid.* **16**, 1282 (1977); J. Boguta and A. R. Bodmer, Nucl. Phys. **A292**, 413 (1977); R. Brockmann, Phys. Rev. C **18**, 1510 (1978); J. Boguta and J. Rafelski, Phys. Lett. **71B**, 22 (1977).

[2]C. J. Horowitz and B. D. Serot, Nucl. Phys. **A368**, 503 (1981).

[3]B. D. Serot and J. D. Walecka, in *Advances in Nuclear Physics,* edited by J. W. Negele and E. Vogt (Plenum, New York, 1986), Vol. 16, and references contained therein.

[4]L. G. Arnold *et al.*, Phys. Rev. C **19**, 917 (1979); L. G. Arnold *et al.*, *ibid.* **23**, 1949 (1981); J. R. Shepard *et al.*, Phys. Rev. Lett. **50**, 1443 (1983). A summary of relativistic Brueckner Hartree-Fock results and related references is given in M. R. Anastasio *et al.*, Phys. Rep. C **100**, 327 (1983).

[5]R. Furnstahl and B. D. Serot, Nucl. Phys. **A468**, 539 (1987).

[6]D. J. Thouless, Nucl. Phys. **22**, 78 (1961); Rep. Prog. Phys. **27**, 53 (1964).

[7]A. L. Fetter and J. D. Walecka, *Quantum Theory of Many-Particle Systems* (McGraw-Hill, New York, 1971).

[8]The code HPLUS2C was made available to the authors by C. Horowitz.

[9]Michael W. Price, Ph.D. thesis, Indiana University, 1986.

[10]R. J. Furnstahl, Ph.D. thesis, Stanford University, 1985; Phys. Lett. **152B**, 313 (1985).

[11]T. de Forest, Jr. and J. D. Walecka, Adv. Nucl. Phys. **15**, 1 (1966).

[12]J. D. Bjorken and S. D. Drell, *Relativistic Quantum Mechanics* (McGraw-Hill, New York, 1964).

[13]T. W. Donnelly and G. E. Walker, Ann. Phys. (N.Y.) **60**, 209 (1970).

[14]J. D. Walecka, in *Muon Physics,* edited by Vernon W. Hughes and C. S. Wu (Academic, New York, 1975).

[15]I. Sick *et al.*, Phys. Rev. Lett. **23**, 1117 (1969).

[16]E. G. Fuller and E. Hayward, in *Nuclear Reactions,* edited by P. M. Endt and P. B. Smith (North-Holland, Amsterdam, 1962), Vol. 11, p. 113.

[17]T. E. Drake, E. L. Tomusiak, and H. S. Caplan, Nucl. Phys. **A118**, 138 (1968).

[18]G. E. Walker, Phys. Rev. C **5**, 1540 (1972).

[19]G. Do Dang, M. Jaminon, and N. Van Giai, Phys. Lett. **153B**, 17 (1985).

[20]H. P. C. Rood, Phys. Rev. C **33**, 1104 (1986).

[21]G. E. Walker, Phys. Rev. C **174**, 1290 (1968). The results for the Serber-Yukawa interaction quoted in this reference have been renormalized to be consistent with the weak interaction coupling constant G used in the present relativistic calculations.

[22]C. Barlow *et al.*, Phys. Lett. **9**, 84 (1964).

[23]M. Eckhouse, Ph.D. thesis, Carnegie Institute of Technology, 1962.

[24]P. A. M. Guichon *et al.*, Phys. Rev. C **19**, 987 (1979).

[25]L. Palffy *et al.*, Phys. Rev. Lett. **34**, 212 (1975).

[26]P. Guichon *et al.*, Z. Phys. A **285**, 183 (1978).

[27]P. A. M. Guichon and C. Samour, Phys. Lett. **82B**, 28 (1979).